1   Response to Anonymous Referee #1

2   --

3   Thank you for your positive comments and suggestions below that have helped to improve the
4   manuscript. All comments are repeated for clarity and the responses to all comments are given
5   in red. We have also appended the revised draft of the manuscript along with this response.
6   All the changes in the manuscript are also colored as red.

8   The main objective of this study is to assess how well TOA SWF can be estimated using OMI
9   cloud and ozone products with a neural network (NN) approach when CERES data are used
10   for training. To meet this objective, information on cloud/aerosol parameters and total column
11   ozone (TCO) from the Aura Ozone Monitoring Instrument (OMI) has been collocated with
12   the Aqua Clouds and Earth's Radiant Energy System (CERES) estimates of TOA SW flux
13   (SWF). The data have been used to develop the NN based estimates of TOA SWF globally
14   (ocean and land) using only OMI data as inputs. The global mean daily TOA SWF calculated
15   from OMI was found to be within ±1% of CERES throughout the year 2007. It is suggested
16   that application of this approach to other ultraviolet sensors, both past and future, may lead to
17   estimates of TOA SWF.

19   **General Comments**

20   1. Not clear what SW parameter at the TOA was used in the regression? Is it the reflected SW
21   or the net SW?

23   The study estimates top-of-the-atmosphere short wave reflected flux (not net), which is the
24   total outgoing flux as derived from CERES measurements. The abstract and introduction
25   have been revised to make this more clear.

27   2. p1, line 26 stated: Application of our neural network to other ultraviolet sensors, both past
28   and future, may provide unique estimates of TOA SWF. This is correct if past sensors have
29   the same type of information on other input parameters as does OMI, which is not the case.

31   This is correct. We have revised the abstract to make it more clear as suggested. We have also
32   removed the word 'unique'. This limitation of the approach is also discussed in the summary
33   section of the paper. The abstract is revised as: "Our derived neural networks can be applied
34   to other sensors, past or future, to estimate TOA SWF, as long all of the necessary input
35   parameters are available."

37   3. p3, line 21 stated: In this study, we utilize OMI cloud, and ozone products along with other
38   ancillary data to estimate TOA SWF. In the title, it is emphasized that what is unique about

this approach is that UV satellite data are used. In what is actually done, no UV data are used directly; information on ozone is used that could come from any source. There is a need to explain what is unique about the approach since it could be repeated with information on these parameters from any other source.

This study primarily uses retrievals and measurements coming from the OMI sensor, which operates in the UV part of the solar spectrum. We use cloud, aerosol, ozone, and LER as inputs to estimate TOA SWF estimates similar to the CERES product. The strength of this approach is to make use of UV measurements/retrieved parameters to estimate TOA SWF, which largely comes from the visible and NIR parts of solar spectrum. We have revised the text to make it more clear as:

"One objective of this study is to assess how well TOA SWF can be estimated using OMI-derived cloud and ozone products with NNs when nearly coincident CERES data are used for training. The developed NNs can then be applied to other data sets with similar products and accuracy. Alternatively, the general training approach could be applied with similar data sets such as with MODIS cloud and ozone products."

We also have revised the title to remove the emphasis on UV as "**Top-of-the-atmosphere shortwave flux estimation from satellite observations: An empirical neural network approach applied with data from the A-train constellation**"

4. p4, line 14 stated: We primarily use 2007 data over global oceans for the training, testing, and validation of neural network models. Since the treatment of surface albedo over oceans and over land is so drastically different, something needs to be said on the impact of such differences and why NNs trained over oceans will perform well over land.

We train the land and ocean NN model independently. The land model uses broadband surface albedo to characterize the land surface whereas winds and chlorophyll are used in the ocean model. Most of the testing and optimization of the NN models was done over ocean. We changed the above sentence to "For general testing and optimization of the neural network models, we primarily use 2007 data over global oceans."

We have added following text to the CERES data section (2.2.1). "We also used broadband surface albedo over land derived using measurements from MODIS and CERES as inputs to the NN trained specifically for land." Also section 4.4 has been modified for clarity.

5. p3-4, line 31 stated: The ADMs heavily depend upon the observed scene type and are sensitive to surface characteristics as well as cloud and aerosol optical properties. This is a

very important issue that the Authors did not address. CERES is using ADMs to derive fluxes at the TOA from the radiances. In the proposed approach, radiances are computed. To compare it to the CERES product, the radiances need to be converted to fluxes. How is it done without the use of ADMs?

The ADMs are indeed very important in estimating flux from radiance measurements and the CERES algorithm follows that method. In our approach, we do not use radiances, ADMs, or scene identification. Our neural network (NN) approach allows us to calculate directly the TOA SW flux without using or calculating broadband radiances. We have used the NN models with inputs from OMI retrievals and trained them to produce TOA SWF flux equivalent to CERES fluxes directly without any intermediate products or tools as shown in Fig. 3.

Page 3 mostly discusses the data sets and CERES approach of estimating fluxes. We discuss our approach in section 3.1, 'General NN architecture and training approach'. We added in the introduction "In essence, the trained NNs have learned or incorporated all of the complexity that is essential to the CERES algorithms (ADMs, scene identification, etc.), and are then able to predict TOA SWF directly and efficiently based on a limited number of retrieved products from OMI or other sensors that provide similar data."

6. CERES provides daily values that are computed with the help of observations from geostationary satellites. How do the Authors get their daily values so a reasonable comparison can be made with the CERES daily values?

We use the CERES SSF product, which contains instantaneous flux values, not daily mean values. The OMI derived flux values are also instantaneous values. We have modified data section to reflect this more clearly. We also provide references, which discuss the SSF product and algorithm in detail.

7. Another important issue that was not explained is related to the selection of clear cases from cloudy cases. How exactly do the Authors decide what scene is clear? They do touch upon the method used by CERES to select clear cases but not for OMI.

Our NN method does not require scene identification. Our training data sets include both clear and cloudy pixels, and the NN estimates TOA SWF for all sky conditions (irrespective of whether the scene is cloudy or clear). No differentiation between clear and cloudy is made in either the training or validation. We do use a separate NN for ECF= 1.0; (Section 3.4) these are cases where the OMI effective cloud fraction is saturated and therefore the Lambertian-equivalent reflectivity (LER) becomes the primary TOA SWF predictor.

8. p6, line 20 stated: The assumed cloud optical depth of 20 is spectrally-independent within the 320-1400 nm wavelength range What about COD of less than 20?

COD of less than 20 at the same geometrical cloud fraction leads to a lower value of the effective cloud fraction. However the spectral variations of ECF remain similar to that shown in Fig. 1. The weak spectral dependence of ECF is explained by that the Lambertian cloud model with cloud reflectivity of 80% effectively accounts for Rayleigh scattering in partially cloudy scenes as it has been shown by Ahmad et al. (2004). We added this explanation and the reference to the text.

Ahmad, Z., Bhartia, P. K., and Krotkov, N.: Spectral properties of backscattered UV radiation in cloudy atmo- spheres, J. Geophys. Res., 109, D01201, doi:10.1029/2003JD003395, 2004.

9. p7, line 26 stated: OMI and CERES collocated pixels are only included in our training and validation samples when the distance between centers of OMI and CERES pixels is less than 20km. At such spatial differences, can one assume that what is clear for one type of observations would be also clear for the other?

It is likely that in many cases OMI and CERES pixels are not observing same scene for a given viewing geometry. This results in collocation "noise". With a sufficiently large sample, the noise essentially averages out and it does not appear to impact NN performance (note that we do not require any pixels to be explicitly clear). We discuss (old Page 12, Line 26 -) that pixel level results are noisier than gridded data, and we attribute this to larger "noise" in the pixel level collocation, which averages out in the gridded product. We added here that "This collocation noise averages out over larger spatial and temporal scales."

10. p8, line3 stated: We also mask OMI pixels with AI > 1 to avoid heavy absorbing aerosol loaded scenes where the fc and OCP are known to contain errors If this is the case, how well will the algorithm perform when there are heavy aerosols in the atmosphere?

The AI>1 threshold only masks pixels with heavy absorbing type of aerosols. It does not include non-absorbing aerosols. Non-absorbing aerosols are essentially treated as clouds within the OMI cloud data sets. We have modified text in section 2.2 to reflect this explicitly.

We do see some differences (biases) with respect to CERES in the results where absorbing aerosols are present (AI is positive but less than 1) and these are discussed on Page 12 – Line 15, Page 12 – Line 29 onward and also, Page 13, Line 25. The bias is difficult to quantify in the presence of heavy absorbing aerosols, because we don't know how well CERES does in this case.

11. The regression equations derived are not presented. What do they look like? They should be provided so that others can use them.

Our method uses NN models to calculate TOA SWF fluxes with a multiple layer architecture and different weighting functions (Figure 3). These are not simple regression models. We will provide the python code for the trained NN models as supplementary material. This code can be used to derive TOA SWF flux provided the appropriate inputs are applied as discussed in the paper.

Specific Comments

1. p1, line 19 stated: The A-train constellation of satellites provides a unique opportunity to analyze near simultaneous data from several of these sensors. What exactly is near-simultaneous? ¼ of an hour can make a large difference in the reflected SW at the TOA.

We changed "near-simultaneous" to "that makes measurements within approximately 15 minutes of each other". We further explain this in section 2 (Page 4, Line 11).

2. p2, line 24 stated: Although CERES provides state-of-art estimates of TOA radiative fluxes, it is not designed to make measurements of individual atmospheric components that impact those fluxes. This was not the objective of CERES to measure individual atmospheric components so it should not be held against CERES. This comment is not a good argument for the case at hand.

We have revised the paragraph as follows to make it clearer. "Continuous and coincident measurements of radiative fluxes and atmospheric components facilitate research studies to estimate and understand the role of different atmospheric components on the planetary energy balance. Although CERES provides state-of-art estimates of TOA radiative fluxes, it was not designed to make measurements of individual atmospheric components that impact those fluxes."

3. Not clear why figure 1 is needed and what it exactly means.

The purpose of Figure 1 is to demonstrate that effective cloud fraction (ECF) is spectrally independent. The near spectral invariance of ECF suggests that it will be highly correlated with TOA SWF and thus a good predictor in a statistical model of TOA SWF. Therefore, this

figure justifies the use of ECF from OMI to predict TOA SWF fluxes. We rearranged this paragraph and provide some additions to make this more clear. We provide further explanation on Page 7, Line 4-10.

4. In most figures, the legends are not sufficiently informative.

We have revised captions of several figures to provide additional information.

5. Also not clear what is compared to what like for example, figure 3. CERES gives flux while OMI is something else.

We believe you are referring to Fig. 2 and not Fig. 3. We added "showing a highly linear relationship" and other information to indicate in the caption that we are not making a direct (apples to apples) comparison.

6. In figure 4 when the difference is taken one can see some striping. Such features usually represent differences in sampling. Needs to be explained.

You are referring to the striping in the southern hemisphere, we believe. In the first paragraph of Sect. 4.3, we address this specifically in reference to Fig. 10, "The striped pattern in the southern hemisphere (latitudes >40S) is mainly associated with high viewing zenith angles in conjunction with high solar zenith angles that occur on one side of the OMI swath." We have now provided a forward reference to that section in the discussion of Fig. 4.

7. Each figure needs to clearly indicate what time averaging is used.

We have revised figure captions to include this information.

In summary, this manuscript requires additional work before being considered for publication.

We have revised the manuscript by following the recommendations made here. We have also revised some of the figures for clarity. We believe that we have addressed all the comments

1 **Top-of-the-atmosphere shortwave flux estimation from satellite observations: An**

2 **empirical neural network approach applied with data from the A-train constellation**

4 Pawan Gupta[1,2], Joanna Joiner[2], Alexander Vasilkov[3,2], P. K. Bhartia[2]

6 [1] {Universities Space Research Association, Greenbelt, MD}
7 [2] {NASA Goddard Space Flight Center, Greenbelt, MD}
8 [3] {Science Systems and Applications, Inc., Greenbelt, MD}

10 Correspondence to: Pawan Gupta (pawan.gupta@nasa.gov)

12 **Abstract**

13 Estimates of top of the atmosphere (TOA) radiative flux are essential for the understanding of
14 Earth's energy budget and climate system. Clouds, aerosols, water vapor, and ozone (O_3) are
15 among the most important atmospheric agents impacting the Earth's short-wave (SW)
16 radiation budget. There are several sensors in orbit that provide independent information
17 related to these parameters. Having coincident information from these sensors is important for
18 understanding their potential contributions. The A-train constellation of satellites provides a
19 unique opportunity to analyze data from several of these sensors. In this paper, retrievals of
20 cloud/aerosol parameters and total column ozone (TCO) from the Aura Ozone Monitoring
21 Instrument (OMI) have been collocated with the Aqua Clouds and Earth's Radiant Energy
22 System (CERES) estimates of total reflected TOA outgoing SW flux (SWF). We use these
23 data to develop a variety of neural networks that estimate TOA SWF globally over ocean and
24 land using only OMI data and other ancillary information as inputs and CERES TOA SWF as
25 the output for training purposes. OMI-estimated TOA SWF from the trained neural networks
26 reproduces independent CERES data with high fidelity. The global mean daily TOA SWF
27 calculated from OMI is consistently within ±1% of CERES throughout the year 2007.
28 Application of our neural network method to other sensors that provide similar retrieved
29 parameters, both past and future, can produce similar estimates TOA SWF. For example, the

well-calibrated Total Ozone Mapping Spectrometer (TOMS) series could provide estimates of TOA SWF dating back to late 1978.

1   Introduction

The Earth's energy budget constrains the general circulation of the atmosphere and determines the climate of the Earth-Atmosphere system; it is therefore also an indicator of possible climate changes (Hatzianastassiou, et al., 2004). There is a long history of attempts to estimate Earth's albedo and energy budget (Dines, 1917; Hartmann et al., 1986). With the advent of the satellite remote sensing era, it became possible to directly measure the albedo of the Earth. Subsequently, the shortwave energy balance at the TOA and the role of clouds, aerosols, and trace gases has been studied using satellite measurements (Ramanathan et al., 1989; Yu et al., 2006; Bellouin et al., 2005; Loeb et al., 2005; Patadia et al., 2008; Joiner et al., 2009).

The Earth Radiation Budget Experiment (ERBE) was launched in October 1984 by the space shuttle Challenger and provided long- and short-wave (SW) radiation parameter measurements. Top-of-atmosphere short-wave (TOA SW) radiative parameter estimates from ERBE (Barkstrom, 1984), Barkstrom and Smith (1986) showed that clouds approximately double the albedo of Earth to all-sky value of 0.3 from an estimated clear-sky value of 0.15 (Ramanathan et al., 1989; Harrison et al., 1990). The next generation of broadband instruments, the Cloud and the Earth's Radiant Energy System (CERES), draws heavily on ERBE heritage. Since its first launch in 1997 onboard the NASA Tropical Rainfall Measurement Mission (TRMM), CERES has provided continuous observations that can be used to understand the role of clouds and the energy cycle in global climate change (Wielicki et al., 1995; Loeb et al., 2012).

Continuous and coincident measurements of radiative fluxes and atmospheric components facilitate research studies to estimate and understand the role of different atmospheric components on the planetary energy balance. Although CERES provides state-of-art estimates of TOA radiative fluxes, it was not designed to make measurements of individual atmospheric components that impact those fluxes. Several studies have utilized aerosol and cloud information from high spatial resolution MODerate resolution Imaging Spectroradiometer (MODIS) measurements to quantify their impact on TOA fluxes (Yu et al., 2006; Patadia et al., 2008; Zhang et al., 2005b; Loeb et al., 2005; Oreopoulos et al., 2009). Several-attempts

have also been made to convert narrowband radiances into broadband fluxes using regression or more sophisticated statistical approaches (Chevallier et al., 1998; Hu et al., 2002; Domenech and Wehr 2011; Vázquez-Navarro et al., 2012).

The Ozone Monitoring Instrument (OMI), flying on NASA's Aura satellite since 2004, provides information about components important for the Earth's SW radiation budget including the effective cloud/aerosol fraction (Stammes et al., 2008; Joiner and Vasilkov, 2006) and total column ozone (TCO) (Veefkind et al., 2006; McPeters et al., 2008; Kroon et al., 2008). OMI-retrieved parameters can be utilized to understand their role in the Earth's SW energy budget.

To model the spatial and temporal distribution of the TOA short-wave flux (SWF) requires a description of the components that control the transfer of solar radiation within the Earth-atmosphere system. When required parameters are missing or incomplete, a statistical approach is an alternative for estimation of TOA SWF. Here, we develop an artificial neural network (NN) model to estimate total reflected TOA outgoing SWF. Artificial NNs are algorithms that simulate biological neural networks by learning and pattern recognition (Bishop, 1995). NNs have been used by many scientific disciplines, including Earth science, to identify patterns and extract trends in imprecise and complicated non-linear data (e.g., Lee et al., 1990; Gupta and Christopher, 2009). In radiation studies, NNs have been used to estimate TOA and surface SWF based on radiative transfer calculations with or without data from satellites (e.g., Krasnopolsky et al., 2008, 2010; Takenaka et al., 2011; Vázquez-Navarro et al., 2012; Jiang et al., 2014). CERES TOA flux algorithms have also used NNs to generate Angular Distribution Models (ADMs) in the absence of sufficient high-resolution imager information for reliable scene identification (Loukachine and Loeb, 2003; 2004).

In this study, we utilize OMI cloud and ozone products along with other ancillary data to estimate TOA SWF. We develop NNs that take OMI-derived quantities as inputs and provide CERES-equivalent TOA SWF as the output. In essence, the trained NNs have learned or incorporated all of the complexity that is essential to the CERES algorithms (ADMs, scene identification, etc.) and are then able to predict TOA SWF directly and efficiently based on a limited number of retrieved products from OMI or sensors that provide similar data. The trained NN models are optimized to run with data sets from OMI or similar sensors and can be applied generally to different seasons and years. For example, the neural network-based models we develop here can be applied to similar measurements from the Total Ozone

Mapping Spectrometer (TOMS) instruments. One objective of this study is to assess how well TOA SWF can be estimated using OMI-derived cloud and ozone products with NNs when nearly coincident CERES data are used for training. The developed NNs can then be applied to other data sets with similar products and accuracy. Alternatively, the general training approach could be applied with similar data sets such as with MODIS cloud and ozone products.

The strength of a NN approach is that it is highly efficient and if well-trained, should be precise and accurate for this type of problem. NNs may be used to examine the sensitivity of TOA SWF to various input data sets, but do not themselves provide specific insight on the physical mechanisms behind those sensitivities. NNs will of course only be as good as the data that are used for training. In addition, they may not perform well for unusual conditions that are not present in the training data set. Therefore, NNs cannot replace dedicated TOA SWF estimates from instruments like CERES.

The paper is organized as follows: Section 2 describes the various satellite data sets utilized in the study. Section 3 discusses the development of NN models including the selection of input parameters. Section 4 evaluates our NN estimation of TOA SWF using independent CERES data over ocean and land. Section 5 summarizes the results and discusses future work.

2   Satellite Data Sets and Coincident Sampling

Under clear-sky conditions, TOA SWF is affected by the Earth's surface properties, atmospheric absorbers such as water vapor, ozone, and aerosols, and scattering by air molecules and particulates. Over ocean, surface properties can be characterized by ocean color and roughness of the ocean surface. Under cloudy sky conditions, cloud optical properties such as the cloud optical thickness, geometrical cloud fraction, effective radius, and phase function affect TOA SWF. In clear and cloudy skies, the solar zenith angle (SZA) and Sun-Earth distance (SED) impact the TOA SWF.

In this work, we make use of data sets mainly from two passive sensors in A-train constellation of satellites that fly within 15 minutes of each other: 1) Aura OMI with an equatorial crossing time of ~13:45 ± 15 minutes local time and 2) Aqua CERES with an equatorial crossing time of ~13:30 local time. For testing and optimization of the neural network models, we primarily use 2007 data over global oceans. Starting around 2008, OMI experienced an anomaly presumably due to material outside the sensor that adversely affects

the quality of the level 1B and level 2 data products in a portion of its 60 rows across the swath. Our study focuses on data in 2007 that are not significantly affected by these anomalies.

2.1.1 CERES

The first CERES instrument flew on the TRMM satellite, launched in November 1997, and provided data until 2000. Five CERES instruments are currently operating; two on NASA's Terra satellite (FM1 and FM2), two on NASA's Aqua satellite (FM3 and FM4), and one on the Suomi National Polar-orbiting Partnership (NPP) satellite (FM5). These CERES instruments provide radiometric measurements of the Earth's atmosphere from three broadband channels: 1) A shortwave channel to measure reflected sunlight (0.3-5 μm), 2) a long wave channel to measure Earth-emitted thermal radiation in the window region (8-12 μm), and 3) a total channel to measure radiation from 0.3 to 200 μm.

CERES radiances are converted to TOA fluxes using angular dependent models (ADMs). The CERES science team has an extensive database of ADM's for clear- and cloudy-sky over both land and ocean (Loeb et al., 2005). The ADMs heavily depend upon the observed scene type and are sensitive to surface characteristics as well as cloud and aerosol optical properties (Loeb et al., 2003; Zhang et al., 2005a; Patadia et al., 2011). The ADMs over ocean are dependent upon wind speed and aerosol optical thickness along with sun-satellite geometry (Zhang et al., 2005a).

The Aqua spacecraft carries two identical CERES instruments: one operates in a cross-track scan mode (FM3) and the other in a biaxial scan mode (FM4). Measurements from the biaxial scan mode were used to develop the ADMs; this provided considerable improvement over the previous generation of instruments including the ERBE (Loeb et al., 2003; 2007).

This study uses the Single Scanner Footprint (SSF, Edition 3A) TOA SWF obtained from the Aqua CERES FM3. The SSF product is an instantaneous merge of CERES parameters with coincident cloud and aerosol parameters derived from the Aqua MODIS (Loeb et al., 2003) at the footprint level (i.e., not daily averages). The high-resolution (1x1 km^2 at nadir) MODIS imager data are used to characterize the clear and cloudy portions of the larger CERES pixel (20x20 km^2 at nadir). We also used broadband surface albedo over land derived using measurements from MODIS and CERES to characterize the land surface in the NN trained specifically over land.

2.2   OMI

OMI provides hyper-spectral measurements of Earth-backscattered sunlight from UV to visible wavelengths (~270-500 nm) with a spectral resolution of the order of 0.5 nm (Levelt et al., 2006). Its spatial resolution is 13x24 km^2 at nadir with a swath width of about 2600 km. Cloud, aerosol, and total column ozone (TCO) products from OMI are used in this study. Specifically, the cloud-aerosol Optical Centroid Pressure (OCP), effective cloud fraction (f_c), Lambertian-Equivalent Reflectivity (LER) at 354.1 nm, Solar Zenith Angle (SZA), Relative Azimuth Angle (RAA), and Viewing Zenith Angle (VZA) are obtained from the OMI cloud products as detailed below, and Aerosol Index (AI) and TCO are obtained from the OMI-TOMS total ozone product (OMTO3, version 8.5, collection 3) (McPeters et al., 2008).

Cloud-aerosol OCP, also known as effective cloud pressure, is a measure of the reflectance-weighted pressure reached by incoming solar photons (Joiner et al., 2012). It is distinct from the cloud-top pressure (CTP). While CTP is the more important parameter needed for TOA long-wave flux, OCP is more related to atmospheric absorption in the short-wave. OCP is derived from OMI observations using two different methods (Stammes et al., 2008): 1) filling-in of solar Fraunhofer lines from rotational-Raman (RR) scattering in the UV (the OMCLDRR product) (Joiner and Bhartia, 1995; Joiner et al., 2004) and 2) collision-induced oxygen absorption (O_2-O_2) at 477 nm (the OMCLDO2 product) (Stammes et al., 2008; Acarreta et al., 2004). Unless otherwise specified, we use the f_c and OCP from OMCLDRR product here.

OMI cloud and trace-gas algorithms use a simplified mixed Lambertian cloud model to estimate observed radiances I_m. In this scenario, a pixel is modeled as a having components from clear and cloudy sub-pixels weighted using an effective cloud fraction f_c, i.e.,

$$I_m = I_g (1 - f_c) + I_c f_c \tag{1}$$

where I_g and I_c are the radiances computed in the Rayleigh atmosphere for Lambertian surfaces corresponding to the clear and cloudy portions of the scene, respectively; f_c is defined as the fraction of the Lambertian cloud covering the pixel and is related to both the geometric cloud fraction and cloud optical thickness. It contains information similar to the Lambertian-equivalent reflectivity of the scene (related to cloud and surface reflectivities). However, because it attempts to account for variations in the Earth's surface reflectivity, it is a more spectrally invariant quantity and therefore potentially more highly correlated with TOA SWF.

1   Formally, the effective cloud fraction is wavelength-dependent because it is defined by

2   spectral quantities (Stammes et al., 2008). We conducted a simulation experiment to evaluate

3   the wavelength dependence of f_c. In this experiment, we simulate observed TOA radiances as

4   a weighted sum of the clear-sky and cloudy radiances, i.e.,

$$I_m = I_g \left(1 - f_g\right) + I_c f_g \qquad\qquad (2)$$

5   where I_c is the cloudy radiance computed with a plane-parallel cloud model that depends on

6   cloud optical thickness, and f_g is the geometrical cloud fraction. In our simulation, clouds

7   have a vertically uniform distribution of the extinction coefficient and phase function. We use

8   a cloud top height of 5 km and a cloud layer thickness of 1 km. The assumed cloud optical

9   depth (COD) of 20 is spectrally-independent within the 320-1400 nm wavelength range. The

10   spectrally-independent optical thickness is a good approximation for clouds with sufficiently

11   large particles (Deirmendjian, 1969). We neglect gaseous absorption in the specified spectral

12   range. Three models of cloud phase function are used: 1) ice crystals with an effective

13   diameter of 60 µm (Baum et al., 2014), 2) Deirmendjian's C1 model of a water cloud having

14   droplets with an effective diameter of 12 µm (Deirmendjian, 1969), and 3) the Henyey-

15   Greenstein (HG) model (e.g. van de Hulst and Irvine, 1963) with an asymmetry parameter of

16   0.85. We use a simplified model of the spectral ground reflectance: R_g = 0.05 at λ<700 µm, R_g

17   = 0.2 at λ>700 µm. We then calculate f_c by inverting Eq. 1 assuming a Lambertian cloud with

18   a reflectivity of 0.8; this is commonly used for trace-gas algorithms (Stammes et al., 2008).

19   If f_c does not vary much with wavelength, then it should be be highly correlated with TOA

20   SWF and thus a good predictor in a statistical model of TOA SWF. We investigate the

21   spectral dependence of f_c in Fig. 1 where we performed calculations using f_g =0.5, SZA = 45^0,

22   and at nadir for the three phase functions assuming a cloud single scattering albedo of unity. It

23   can be seen that f_c is nearly invariant with wavelength over a wide spectral range; it changes

24   by only a few percent even for the steep change in the ground reflectance (simulating the so-

25   called red-edge) at 700 nm. COD of less than 20 at the same geometrical cloud fraction leads

26   to a lower value of the effective cloud fraction. However the spectral variations of ECF

27   remain similar to that shown in Fig. 1. The weak spectral dependence of ECF is explained by

28   the fact that the Lambertian cloud model with cloud reflectivity of 80% effectively accounts

29   for Rayleigh scattering in partially cloudy scenes as it has been shown by Ahmad et al.

30   (2004). This result holds when other input parameters in our simulation are varied. We will

31   show the implications of the spectral invariance of f_c below.

We have used the following modified cloud fraction parameter, f_{c_mod}, as a predictor to estimate TOA short wave flux:

$$f_{c\_mod} = f_c \times \cos(SZA) \times \left(1/_{SED^2} \right)$$

where SED is the sun-Earth distance. The modification accounts for variation in the incoming solar irradiance with respect to SZA and SED. Figure 2 shows a 2D histogram for a month of collocated CERES TOA SWF and OMI f_{c_mod} (collocation criteria described in detail below) that demonstrates the near linear relationship between the two parameters. It also indicates that the single parameter f_{c_mod} captures much of the variability in TOA SWF.

2.3 Ancillary Data

In addition to OMI data, a SeaWiFs-derived chlorophyll concentration (Chl) climatology is used as an input predictor when $f_c < 1$. The precipitable water (PW) and 2 m surface wind speed (Wind) are also used as predictors; these are provided in the CERES SSF data set and are taken from the Goddard Earth Observing System (GEOS) 4 reanalysis (Bloom et al., 2005).

2.4 Coincident Sampling of OMI and CERES

Because the sizes of the OMI (13 km x 24 km) and CERES (20 km^2) pixels are similar at nadir, we perform a simple spatial collocation by finding the closest CERES pixel corresponding to each OMI pixel. OMI and CERES collocated pixels are only included in our training and validation samples when the distance between centers of OMI and CERES pixels is less than 20 km. We do not include pixels with viewing zenith angles > 60°. At these angles, OMI and CERES pixels become significantly larger (~150 km for OMI and ~200 km for CERES in the cross track direction) and therefore may contain many different scene types. We also mask OMI pixels with AI > 1 to avoid heavy absorbing aerosol loaded scenes where the f_c and OCP are known to contain errors (Vasilkov et al., 2008). This does remove not non-absorbing aerosols. Non-absorbing aerosols are essentially treated as clouds within the OMI cloud data sets. We examined the frequency distribution of the distance between OMI and CERES pixels of all the collocated data sets and found that most of the collocated data, 98% and 60%, have distances less than 20km and 10km, respectively. The quality-controlled collocated data are then averaged on equal latitude and longitude grids of 1° x 1° (unless otherwise specified) for training, testing, and validation of the neural networks.

The NN inputs (predominantly retrievals from OMI measurements) are used train the NN to match the output (CERES-derived TOA SWF). Once the network is trained, input data sets can be used to calculate TOA SWF with characteristics similar to the CERES product. Therefore, the NN produced TOA SWF flux will be referred as OMI estimated SWF throughout the manuscript.

3 Artificial Neural Network Model

3.1 General NN architecture and training approach

The general neural network architecture has three layers of neurons: an input layer, a hidden layer, and an output layer with standard multi-layer network architecture. We use the same number of neurons in the hidden layer as in the input layer as this produced generally good results. The input layer has an identity activation function; all other layers are connected by sigmoid activation functions (Equation 3).

$$y(x) = \frac{1}{1 + e^{-x}} \tag{3}$$

The network normalizes both input and output data sets with a unique linear mapping for each input and output parameter. Figure 3 provides an example of a schematic of the network used in our study. Here we used two different Neural Network Models (NNMs): one with nine nodes or parameters (NNM1) and a second with seven nodes (NNM2) in the input layer. Both of these models have one node (TOA SWF) in the output layer. Figure 3 also lists the input parameters corresponding to the NNM1 and NNM2 models. The NNM1 model is optimized for ocean cases where the OMI $f_c < 1.0$, whereas NNM2 is optimized for cases where $f_c = 1$ (saturated cases).

NNMs require optimized training to produce accurate outputs. Here we use a standard back propagation training algorithm (Hertz et al., 1991), where inputs are iteratively sent to the neural network. In back propagation, the hidden layer weights associated with each input parameter are modified through the training process that minimizes errors between the targets and outputs (Bishop, 1995; Gardner and Dorling, 1998). After each iteration, the error is propagated backward through the network and weights are modified to bring the actual response of the network closer to the desired output in a statistical sense. The function minimized during the training is a sum of squared errors of each output for each training

1 pattern. Once the network is trained, it can be evaluated using independent data (i.e., not used

2 in the training data set).

3.2   Impact of different input parameters

4 Here we examine the impact of using various input parameters on the derived neural

5 networks. This exercise is performed using data with $f_c < 1$ with one month of the data over

6 ocean (January 2007). Table 1 presents the performance of eight different NNMs, denoted

7 models "a" through "h", with various input parameters listed in Table 1 and described in more

8 detail in sections 3.2.1-3.2.2.

3.2.1   Inclusion of OMI UV-derived parameters

10 In model "a", we have combined the effects of SZA, SED, and f_c into a single input parameter

11 called f_{c_mod}, which was defined in Sect. 2.2. Use of this modified input parameter alone

12 explains about 94% (R=0.97) of the variability in TOA SWF. As we add other parameters in

13 models "b" through "h", we observe small improvements in the OMI-estimated TOA SWF.

14 Figure 4 shows the spatial distribution of monthly mean OMI-CERES SWF differences for

15 these models.

16 The TOA SWF is estimated from a measured radiance and therefore the observational

17 geometry factors in. The addition of satellite viewing geometry parameters (VZA, RAA) to

18 model "a" provides improvements in areas of high biases and reduces the standard deviation

19 from 37.1 Wm^{-2} to 31.4 Wm^{-2}. Model "c" tests the ability of the 354 nm reflectivity (LER) to

20 predict TOA SWF in place of f_{c_mod}. Although the statistical parameters in table 1

21 corresponding to models "b" and "c" are very similar, we note spatial differences in the OMI-

22 CERES TOA SWF in Figure 4. Further analysis reveals that the f_c-based model "b" provides

23 more accurate flux estimation as compared with the LER-based model for a larger range of

24 fluxes.

25 The inclusion of TCO (model "d") as an input parameter positively impacts TOA SWF

26 estimation as shown in Figure 4 (d); the high positive biases in the tropical Pacific and Indian

27 oceans and in the region near 60$^{\text{o}}$N have been reduced. The percentage of monthly mean

28 OMI-CERES data that falls within ±8% increases from 91% in model c to 94% in model "d".

29 Model "e" adds cloud OCP to the input parameters included in model "b". OCP also improves

30 SWF estimates; the regions where improvement occurs are different from those improved by

31 using TCO. Model "f" shows that when TCO and OCP are used together as input parameters,

there is further improvement in SWF estimation. Although the global statistics in Table 1 do not clearly reflect this improvement, Figure 4(f) shows that inclusion of OCP and TCO reduces biases in many regions, most prominently in the tropics. The percentage of total OMI samples (monthly mean) within ±8% of CERES increases from 92% in model "b" to 95% in model "f". Apart from these parameters, we also evaluated the inclusion of AI as an input parameter (not shown here). We found that overall it does not significantly improve the results; however it does provide some improvement in regions with positive AI values.

3.2.2 Addition of meteorological and other ancillary data

The impact of surface winds and total column water vapor (model "g" in Figure 4g) is more prominent in the tropics than in other regions. Inclusion of chlorophyll and LERs in model "h" removes some of the notable low biases in TOA SWF near the coast of Northern China, Caspian Sea, and Black Sea. Furthermore, model "h" corrects for negative biases in areas with high TOA SWFs, most likely due to the inclusion of LER. The model "h" produces 89% (99%) of OMI-estimated monthly mean TOA SWFs within ±5% (±12%) of CERES and is best of the eight models. In all of the results, some striped patterns appear in the difference maps. These stripes are also seen in difference maps for July and will be discussed below in Sect. 4.3.

3.3 Consistency over time

We next examine the performance of the NN model "h" with respect to different input samples. We first examine the robustness of the NN for detection of inter-annual variability. In this exercise, we trained the NN with data from the first 15 days of January 2007 as above, and applied it to input data from the entire months of January 2007 (Figure 5a) and January 2006 (Figure 5b). Figure 5(a-b) presents 2D histograms similar to that in Figure 2 but here compares the TOA SWF from the NN with that from CERES for January of the two different years over ocean. The colors represent the 2D histogram (or density) of coincident pairs using a bin size of 10 Wm^{-2}. The solid black 1 to 1 line is shown with three dotted lines on both sides that represent envelopes of ±5%, ±10%, and ±15% OMI-CERES differences. Figure 5(a-b) shows that the NN performance is consistent between years. Although the number of samples in January of 2006 and 2007 is a bit different, the NN model produces similar statistics.

A NN trained on one particular month of data is not guaranteed to perform well for a different month. In the next test, we used the NN model trained on January 2007 data with input data from July 2007. Results for July (using CERES as the benchmark) were degraded as compared with application to January data. This is due presumably to changes in observing conditions between the two different months (changes in solar angles).

We then trained the same NN (identical input parameters) using a subset of data from July 2007 and applied it to data from the entire month of July 2007. Results (again using CERES as the benchmark) were of similar quality to those where the NN was trained and applied to January. This exercise suggests that we may need to use different models for different months or expand our training data set for application to different months.

We next use data from the 1st day of each month of 2007 for training and data from the 16th day of each month of 2007 for evaluation. The comparisons with CERES using the training and validation data are consistent as shown in Figure 6. The almost identical values of statistical parameters for training and validation data demonstrate that the neural network has been well trained. For example, there is a high degree of linear correlation (R = 0.98 or R^2 =0.96) and slopes close to 1 (0.96) in both training and validation comparisons. The mean bias in both training and validation data sets is close to zero whereas the global standard deviation remains stable and close to 30 Wm^{-2} in the two independent model runs. Further analysis shows that 83%, 70% and 43% of TOA SWF estimated from OMI (training and validation data combine) lie within the 15%, 10%, and 5% of the CERES TOA SWF, respectively.

Further evaluation of the entire year reveals that this NN (model "h") is appropriate for all months. Therefore this model will be used for subsequent analyses in this study. Creating more networks as a function of scene type or for different latitude belts or even for different months/seasons may improve results in certain regions. However, based on our results, we simplified the approach by minimizing the number of networks.

3.4 Case of $f_c = 1$

About 1-2 % of total coincident data correspond to $f_c = 1$, typical of overcast conditions with optically thick clouds. These cases were modeled using a simpler NN model with inputs of LER, SZA, VZA, RAA, OCP, O3, and PW; the surface-related parameters (surface wind speed and chlorophyll content) do not produce a significant impact for ECF=1 and have

1 therefore been removed. Subsequent all-sky results shown in Fig. 6 use combined outputs
2 from the two separate models for $f_c < 1$ and $f_c = 1$.

4 Results and Discussion

4.1 Bias and RMSE as a function of effective cloud fraction

5 Here onward, all the results presented in Figures 7-12 and discussed are produced using
6 model "h", which is the most optimized model. Figure 7 presents the Root Mean Square Error
7 (RMSE), RMSE Normalized by CERES flux (NRMSE in %), data sample (%), and bias (%)
8 for 5% ECF bins. This analysis includes both training and validation data as presented in
9 Figure 6. The RMSE varies between about 24-35 Wm^{-2} and continuously increases with cloud
10 fraction (and observed TOA SW flux). The NRMSE, on the other hand, continuously
11 decreases with ECF from about 18% for 5% ECF to ~6% for overcast conditions. The bias
12 represents the mean error (in %) for each ECF bin. The mean global bias shows more
13 variability than RMSE and is highest (2.9%) for about 10% ECF. The bias decreases sharply
14 from 2.9% at $f_c = 0.1$ to about 1.2% at $f_c = 0.4$. The bias remains low (<1.2%) for $f_c > 0.4$
15 (usually associated with frontal or deep convective clouds). The higher biases for lower f_c
16 (usually associated with thin cirrus and broken clouds) are likely related to higher noise and
17 uncertainties in OMI cloud parameters. For example, Joiner et al., (2012) showed that cloud
18 OCP errors increase with decreasing f_c. The biases may also be related to absorbing aerosol in
19 the scene, particularly when it overlies clouds. This will be illustrated in more detail below as
20 we show spatial variations in OMI-CERES differences.

4.2 Effects of Spatial and Temporal Averaging

22 In order to evaluate the NN performance at different spatial and temporal scales similar to
23 those used by the climate community, we use data from July 2007. Figure 8 presents a
24 comparison of daily CERES and OMI TOA SWF over ocean for 6 spatial scales: the OMI
25 native pixel (13x24 km^2 at nadir) and 0.5^o, 1°, 2°, 5°, and 10° gridded spatial resolutions.
26 Statistical parameters for these comparisons are reported in Table 2. As expected, the pixel
27 level data are much noisier than the gridded data owing to collocation noise in partly cloudy
28 cases. This collocation noise averages out over larger spatial and temporal scales. Regardless
29 of the noise, the slope (0.96) is still close to 1, and the linear correlation coefficient is 0.96
30 with a standard deviation of 47.7 Wm^{-2}. Below 300 Wm^{-2}, where the sample density is
31 highest, the NN slightly underestimates the CERES SWF. The mean bias of the OMI-

1 estimated SWF with respect to CERES is -1.4 Wm^{-2}. This bias may be due to a combination

2 of effects including uncertainties in the input parameters as well as the limitations of the NN

3 model itself. For example, we have excluded pixels with a clear signature of absorbing

4 aerosols (OMI derived AI > 1) where OMI effective cloud fractions and pressures may be in

5 error in both the training and validation data. However, in some regions where smoke and

6 dust overlaying clouds is common (e.g., west coast of Africa), pixels with erroneous cloud

7 fractions owing to small amounts of absorbing aerosol may be present in both the training and

8 validation data. This may produce errors in the NN model and will be examined in more detail

9 below.

10 For the daily data, as the spatial averaging scales increase from 0.5^o to 10°, the OMI-estimated

11 SWF becomes almost identical to CERES; the correlation coefficient increases from 0.97 to

12 0.99, and the slope increases from 0.96 to 0.97. The percentage of OMI data that falls within

13 ±5% of CERES increases from 37% for 0.5^o to 69% for 10° grids. About 87% percent of

14 OMI-estimated 2° gridded daily mean TOA SWFs are within 15% of CERES data.

15 Figure 9(a-d) shows 2D histograms of monthly mean gridded data over ocean at 0.5^o, 1°, 2°,

16 and 5° spatial resolutions, respectively. The monthly inter-comparisons of OMI and CERES

17 SWF show excellent agreement at all spatial resolutions with correlation coefficients of 0.99

18 and slopes of 0.98 (Table 2). The global mean biases vary between -1.8 and 0.25 Wm^{-2}. The

19 standard deviations vary between 6.6 and 12.9 Wm^{-2} for the different spatial resolutions.

20 Ninety seven percent of monthly mean 1° gridded OMI estimated TOA SWFs are within 15%

21 of those derived from CERES, and 93% are within 10%.

22 **4.3   Spatial Distribution of TOA SWFs over ocean**

23 Figure 10 presents the spatial distribution of 1° gridded monthly mean (July 2007) TOA SWF

24 from CERES (Fig. 10a) and the difference with the OMI in Wm^{-2} (Fig. 10b) and percent

25 difference (Fig. 10c). There are subtle differences between the NN and CERES estimates of

26 TOA SWF as shown in Figure 10b and c. The OMI minus CERES histograms (Fig. 10d)

27 show that for 44% (79%) samples, NN fluxes are within ±2 (±5) % of CERES fluxes. About

28 9% of the samples have biases of ±8% or more. Overall, the northern hemisphere shows better

29 agreement than southern hemisphere during July (boreal summer). This could be due to larger

30 errors in the OMI cloud products at higher solar zenith angles in the southern hemisphere. The

31 low biases on the west coast of Africa may be due to the presence of absorbing aerosols,

32 particularly when they occur over clouds. The striped pattern in the southern hemisphere

1   (latitudes > 40$^{\mathrm{o}}$S) is mainly associated with high viewing zenith angles in conjunction with

2   high solar zenith angles that occur on one side of the OMI swath.

3   Figure 11 similarly shows differences between CERES and OMI TOA SWF over ocean

4   derived using f$_{c}$ and OCP from the OMI O2-O2 product in place of the OMI RRS product.

5   Because there are slight differences in the two cloud products, we retrained the network with

6   OMI O2-O2 cloud parameters to be consistent. The use of the O2-O2 f$_{c}$ and OCP improves

7   the accuracy of the estimated TOA SWF. The regions of improvement include the west coasts

8   of South America and southern Africa and some parts of Indian Ocean. The O2-O2 cloud

9   product, which uses visible wavelengths, is less affected by absorbing aerosol; this may

10   explain the improvement in these areas where absorbing aerosol, especially over clouds, is

11   common. However, negative biases remain over large regions off the west coast of Africa.

12   Figure 12a shows a time series of daily global mean values of TOA SWF over ocean from

13   OMI and CERES for 2007. Both instruments show almost identical daily variations with

14   differences within ±1%. Figure 12b, c provides monthly averaged (July 2007) CERES and

15   OMI zonal and meridional means of TOA SWF. The OMI-derived TOA SWF is able to well

16   reproduce the variability shown in the CERES data.

17   **4.4   Spatial Distribution of TOA SWFs over Land**

18   We developed a similar land only NN model that utilizes most of the input parameters from

19   our ocean NN (e.g., OMI RRS cloud parameters). The only change is that for surface

20   characterization, we use a monthly climatology of surface broad-band albedo in place of the

21   chlorophyll concentration and surface wind speed. The albedo product is derived using a

22   combination of CERES and MODIS observations at 1$^{\mathrm{o}}$ spatial resolution (Rutan et al., 2009).

23   The land NN model is trained and validated over land only and it follows a similar approach

24   as was used above over ocean but with the slightly different set of input parameters. We have

25   not performed extended analyses and testing over land as we did over ocean. Here, we

26   demonstrate that the same methodology with different input parameters can reproduce

27   CERES TOA SW flux over land with similar accuracy and precision as was obtained over

28   ocean.

29   Figure 13 shows results from the OMI-derived CERES-trained NN that produces TOA SWF

30   over land. Statistical comparison with CERES over land provides results similar to those over

31   ocean. The NN performs well over Asia and parts of Europe and the Americas. The OMI-

based NN tends to underestimate TOA SWF over the high albedo desert areas of Northern Africa, Australia, and also over some regions of South America. Note that the large differences that occur in coastal regions may be due to imperfect collocations.

5   Summary and Conclusions

We have developed a neural network approach to estimate TOA SWF based primarily on UV parameters retrieved with the Aura OMI and Aqua CERES-derived TOA SWF used for training. One year of data from OMI and CERES has been used to train/validate/analyze several separate neural networks for different conditions, which together provide estimation of TOA SWF under all-sky conditions. The most important input parameters are effective cloud fraction and sun-satellite geometry. Total column ozone and cloud optical centroid pressure from OMI, as well as surface-related parameters, provide secondary positive impacts.

Independent validation at different spatial and temporal scales shows that the OMI NN-based approach reproduces CERES-derived TOA SWF with high fidelity. Correlation coefficients for all comparison are > 0.95, and slopes are close to unity. A high percentage of OMI-estimated monthly mean TOA SWF at 0.5^o spatial resolution over global oceans (97%) falls within 15% of CERES. The global mean bias in pixel level data of about -1.4 Wm^{-2} over oceans with respect to CERES is likely due in part to errors in OMI cloud parameters that occur in the presence of absorbing aerosols.

We plan to apply our derived neural networks to long-term well-calibrated UV measurements from TOMS. The TOMS series provides a long-term data record dating back to late 1978 (about half a decade before the first ERBE launch) with a few small gaps between that time and the first CERES launch. We should be able to apply NN models derived with CERES/OMI to TOMS, provided that the input parameters are either available and compatible or can be estimated independently. For example, in place of actual cloud OCPs that are available from OMI, but not from TOMS, we could use a cloud OCP climatology that was developed from OMI data for use in the TOMS total ozone algorithm. The lower spatial resolution of TOMS is not expected to present any difficulties. This approach can also be extended to the future geostationary missions that provide the relevant input data, such as the NASA Earth Ventures Tropospheric Emissions: Monitoring of Pollution (TEMPO), the Korean Geostationary Environmental Monitoring Spectrometer (GEMS), and the European Space Agency (ESA) Sentinel 4 (Al-Saadi et al., 2015). Finally, we may apply the NN training and evaluation approach to data from CERES and the nadir mapper on the Ozone

Mapping Profiling Suite (OMPS) that provides information similar to OMI. Both instruments fly on the Suomi National Polar Partnership (NPP) satellite. This may reduce collocation noise and small biases that result from the time difference between OMI and CERES measurements.

Acknowledgements

This material is based upon work supported by the National Aeronautics and Space Administration (NASA) issued through the Science Mission Directorate (SMD) for the Aura Science Team managed by Kenneth Jucks and Richard Eckman. We thank the CERES, OMI, MODIS, and GEOS-DAS data processing teams for providing the data used for this study. We would also like to thanks Norman Loeb and Arlindo da Silva for useful discussion and comments during the preparation of manuscript.

References

Acarreta, J. R., De Haan, J. F., and Stammes, P.: Cloud pressure retrieval using the O_2-O_2 absorption band at 477 nm, J. Geophys. Res., 109, D05204, doi:10.1029/2003JD003915, 2004.

Ahmad, Z., Bhartia, P. K., and Krotkov, N.: Spectral properties of backscattered UV radiation in cloudy atmospheres, J. Geophys. Res., 109, D01201, doi:10.1029/2003JD003395, 2004.

Al-Saadi, J., Carmichael, G., Crawford, J., Emmons, L., Song, C-K., Chang, L.-S., Lee G., Kim, J., Park, R.: NASA Contributions to KORUS-AQ: An International Cooperative Air Quality Field Study in Korea, NASA White Paper (https://goo.gl/VhssdX) - accessed on May 3, 2016.

Barkstrom, B. R. and Smith, G. L.: The Earth radiation budget experiment: Science and implementation, Rev. Geophys., 24, 379– 390, 1986.

Barkstrom, B. R.: The Earth radiation budget experiment (ERBE), Bull. Am. Meteorol. Soc., 65, 1110–1185, 1984.

Baum, B. A., Yang, P., Heymsfield, A. J., Bansemer, A., Merrelli, A., Schmitt, C., and Wang, C.: Ice cloud bulk single-scattering property models with the full phase matrix at wavelengths

from 0.2 to 100 µm, J. Quant. Spectrosc. Radiat. Trans., 146, 123-139, doi:10.1016/j.jqsrt.2014.02.029, 2014.

Bellouin, B., Boucher, O., Haywood, J., and Reddy, M. S.: Global estimates of aerosol direct radiative forcing from satellite measurements, Nature, 438, 1138–1140, doi:10.1038/nature04348, 2005.

Bishop, M.: Neural networks for pattern recognition, Oxford University Press, Inc., New York, 1995.

Bloom, S., da Silva, A., and Dee, D.: Technical Report Series on Global Modeling and Data Assimilation, edited by: Suarez, M. J., Documentation and Validation of the Goddard Earth Observing System (GEOS) Data Assimilation System–Version 4, NASA GSFC NASA/TM— 2005–104606, 26, available at: http://gmao.gsfc.nasa.gov/systems/geos4/Bloom.pdf, 2005.

Chevallier, F., Cheruy, F., Scott, N. A., and Chedin, A.: A neural network approach for a fast and accurate computation of a longwave radiative budget, J. Appl. Meteorol., 37, 1385–1397, 1998.

Deirmendjian, D.: Electromagnetic scattering on spherical polydispersions, Elsevir Sci., New York, 290pp, 1969.

Dines, W. H.: The heat balance of the atmosphere, Q. J. R. Meteorol. Soc., 43, 151–158, 1917.

Domenech, C., and Wehr, T.: Use of Artificial Neural Networks to Retrieve TOA SW Radiative Fluxes for the EarthCARE Mission, IEEE Trans. Geosci. Remote Sens., 49, 1839-1849, 2011.

Gardner, M. W., and Dorling, S. R.: Artificial neural networks: A review of applications in the atmospheric sciences, Atmos. Environ., 32, 2627–2636, doi:10.1016/S1352-2310(97)00447-0, 1998.

Gupta, P., and Chirstophe, S. A.: Particulate matter air quality assessment using integrated surface, satellite, and meteorological products: 2. A neural network approach, J. Geophys. Res.,114, D20205, doi:10.1029/2008JD011497, 2009.

Harrison, E. F., Minnis, P., Barkstrom, B. R., Ramanathan, V., Cess, R. D., and Gibson, G. G.: Seasonal variation of cloud radiative forcing derived from the Earth Radiation Budget Experiment, J. Geophys. Res., 95, 18687–18703, 1990.

Hartmann, D. L., Ramanathan, V., Berroir, A., and Hunt, G. E.: Earth radiation budget data and climate research, Rev. Geophys., 24, 439–468, 1986.

Hatzianastassiou, N., Fotiadi, A., Matsoukas, Ch., Pavlakis, K., Drakakis, E., Hatzidimitriou, D., and Vardavas, I.: Long-term global distribution of earth's shortwave radiation budget at the top of atmosphere, Atmos. Chem. Phys., 4, 1217-1235, doi:10.5194/acp-4-1217-2004, 2004.

Hertz, J. A., Krogh, A. S., and Palmer, A.: Introduction to the Theory of Neural Computation, Addison-Wesley, Redwood City, Calif., 1991.

Hu, Y., Zhang, H., Wielicki, B., and Stackhouse, P.: A neural network MODIS-CERES narrowband to broadband conversion, IEEE Geoscience and Remote Sensing Symposium, 3227–32296, 2002.

Jiang, B., Zhang, Y., Liang, S., Zhang, X., and Xiou, Z.: Surface daytime net radiation estimate using artificial neural networks, Remote Sens., 6, 11031-11050, doi:10.3390/rs61111031, 2014.

Joiner, J. and Vasilkov, A. P.: First results from the OMI Rotational Raman Scattering Cloud Pressure Algorithm, IEEE Trans. Geosci. Remote Sens., 44, 1272–1282, 2006.

Joiner, J., and Bhartia, P. K.: The determination of cloud pressures from rotational-Raman scattering in satellite backscatter ultraviolet measurements, J. Geophys. Res., 100, 23,019-23,026, 1995.

Joiner, J., Schoeberl, M. R., Vasilkov, A. P., Oreopoulos, L., Platnick, S., Livesey, N. J., and Levelt, P. F.: Accurate satellite-derived estimates of the tropospheric ozone impact on the global radiation budget, Atmos. Chem. Phys., 9, 4447-4465, doi:10.5194/acp-9-4447-2009, 2009.

Joiner, J., Vasilkov, A. P., Flittner, D. E., Gleason, J. F., and Bhartia, P. K.: Retrieval of cloud chlorophyll content using Raman scattering in GOME spectra, J. Geophys. Res., 109, D01109, doi:10.1029/2003JD003698, 2004.

1 Joiner, J., Vasilkov, A. P., Gupta, P., Bhartia, P. K., Veefkind, P., Sneep, M., de Haan, J.,
2 Polonsky, I., and Spurr, R.: Fast simulators for satellite cloud optical centroid pressure
3 retrievals; evaluation of OMI cloud retrievals, Atmos. Meas. Tech., 5, 529-545,
4 doi:10.5194/amt-5-529-2012, 2012.

5 Krasnopolsky, V. M., Fox-Rabinovitz, and Belochitski, A. A.: Decadal climate simulations
6 using accurate and fast neural network emulation of full, longwave and shortwave, radiation,
7 Month. Weath. Rev., 136, 3683-3695, 2008.

8 Krasnopolsky, V. M., Fox-Rabinovitz, M. S., Hou, Y. T., Lord, S. J., Belochitski, A. A.:
9 Accurate and fast neural network emulations of model radiation for the NCEP coupled
10 climate forecast system: climate simulations and seasonal predictions, Month. Weath. Rev.,
11 138, 1822-1842, 2010.

12 Kroon, M., Veefkind, J. P., Sneep, M., McPeters, R. D., Bhartia, P. K., and Levelt, P. F.:
13 Comparing OMI-TOMS and OMIDOAS total ozone column data, J. Geophys. Res., 113,
14 D16S28, doi:10.1029/2007JD008798, 2008.

15 Lee, J., Weger, R. C., Sengupta, S. K., and Welch, R. M.: A neural network approach to cloud
16 classification, IEEE Trans. Geosci. Remote Sens., 28, 846 -85, 1990.

17 Levelt, P. F., van den Oord, G. H. J., Dobber, M. R., Mälkki, A., Visser, H., de Vries, J.,
18 Stammes, P., Lundell, J. O. V., and Saari, H.: The Ozone Monitoring Instrument, IEEE Trans.
19 Geosci. Remote Sens., 44, 1093–1101, 2006.

20 Loeb, N. G., Manalo-Smith, N., Kato, S., Miller, W. F., Gupta, S. K., Minnis, P., and
21 Wielicki, B. A.: Angular distribution models for top-of-atmosphere radiative flux estimation
22 from the Clouds and the Earth's Radiant Energy System instrument on the Tropical Rainfall
23 Measuring Mission Satellite, Part I: Methodology, J. Appl. Meteorol., 42, 240–265, 2003.

24 Loeb, N. G., and Manalo-Smith, N.: Top-of-Atmosphere direct radiative effect of aerosols
25 over global oceans from merged CERES and MODIS observations, J. Climate, 18, 3506–
26 3526, 2005.

27 Loeb, N. G., Kato, S., Loukachine, K., and Manalo-Smith, N.: Angular distribution models
28 for top-of-atmosphere radiative flux estimation from the Clouds and the Earth's Radiant

Energy System instrument on the Terra Satellite. Part I: Methodology, J. Atmos. Ocean. Tech., 22, 338–351, doi:10.1175/JTECH1712.1, 2005.

Loeb, N. G., Kato, S., Loukachine, K., Manalo-Smith, N., and Doelling, D. R.: Angular distribution models for top-of-atmosphere radiative flux estimation from the Clouds and the Earth's Radiant Energy System instrument on the Terra satellite. Part II: Validation, J. Atmos. Ocean. Tech., 24, 564–584, doi:10.1175/JTECH1983.1, 2007.

Loeb, N. G., Kato, S., Su, W., Wong, T., Rose, F. G., Doelling, D. R., Norris, J. R., and Huang, X.: Advances in understanding top-of-atmosphere radiation variability from satellite observations, Surv. Geophys., 33, 359–385, doi:10.1007/s10712-012-9175-1, 2012.

Loukachine, K., and Loeb, N. G.: Application of an artificial neural network simulation for top-of-atmosphere radiative flux estimation from CERES, J. Atmos. Oceanic Technol., 20, 1749–1757, 2003.

Loukachine, K., and Loeb, N. G.: Top-of-atmosphere flux retrievals from CERES using artificial neural networks, J. Remote Sens. Environ., 93, 381–390, 2004.

McPeters, R. D., Kroon, M., Labow, G. J., Brinksma, E., Balis, D., Petropavlovskikh, I., Veefkind, J. P., Bhartia, P. K., and Levelt, P. F.: Validation of the Aura Ozone Monitoring Instrument Total Column Ozone Product, J. Geophys. Res., 113, D15S14, doi:10.1029/2007JD008802, 2008

Oreopoulos, L., Platnick, S., Hong, G., Yang, P., and Cahalan, R. F.: The shortwave radiative forcing bias of liquid and ice clouds from MODIS observations, Atmos. Chem. Phys., 9, 5865-5875, doi:10.5194/acp-9-5865-2009, 2009.

Patadia, F., Christopher, S. A., and Zhang, J.: Development of empirical angular distribution models for smoke aerosols: Methods, J. Geophys. Res., 116, 1984–2012, 2011.

Patadia, F., Gupta, P., and Christopher, S. A.: First observational estimates of global clear sky shortwave aerosol direct radiative effect over land, Geophys. Res. Lett., 35, L04810, doi:10.1029/2007GL032314, 2008.

Ramanathan, V., Cess, R. D., Harrison, E. F., Minnis, P., Barkstrom, B. R., Ahmad, E., and Hartmann, D.: Cloud radiative forcing and climate: Results from the Earth Radiation Budget Experiment, Science, 243, 57–63, 1989b.

Rutan, D., Rose, F., Roman, M., Manalo-Smith, N., Schaaf, C., and Charlock, T.: Development and assessment of broadband surface albedo from Clouds and the Earth's Radiant Energy System Clouds and Radiation Swath data product, J. Geophys. Res., 114, D08125, doi:10.1029/2008JD010669, 2009.

Stammes, P., Sneep, M., de Haan, J. F., Veefkind, J. P., Wang, P., and Levelt, P. F.: Effective cloud fractions from the Ozone Monitoring Instrument: theoretical framework and validation, J. Geophys. Res., 113, D16S38, doi:10.1029/2007JD008820, 2008.

Takenaka, H., Nakajima, T. Y., Higurashi, A., Higuchi, A., Takamura, T., Pinker, R. T., and Nakajima, T.: Estimation of solar radiation using a neural network based on radiative transfer, J. Geophys. Res., 116, D08215, doi: 10.1029/2009JD013337.

van de Hulst, H. C., Irvine, W. M.: General report on radiation transfer in planets: Scattering in model planetary atmospheres, Mem. Soc. R. Sci. Liege, 7, 78-98, 1963.

Vasilkov, A. P., Joiner, J., Spurr, R., Bhartia, P. K., Levelt, P. F., and Stephens, G.: Evaluation of the OMI cloud pressures derived from rotational Raman scattering by comparisons with other satellite data and radiative transfer simulations, J. Geophys. Res., 113, D15S19, doi:10.1029/2007JD008689, 2008.

Vázquez-Navarro, M., Mayer, B., and Mannstein, H.: A fast method for the retrieval of integrated longwave and shortwave top-of-atmosphere upwelling irradiances from MSG/SEVIRI (RRUMS), Atmos. Meas. Tech., 6, 2627-2640, doi:10.5194/amt-6-2627-2013, 2013.

Veefkind, J. P., de Haan, J. F., Brinksma, E. J., Kroon, M., and Levelt, P. F.: Total ozone from the ozone monitoring instrument (OMI) using the DOAS technique, IEEE Trans. Geosci. Remote Sens., 44, 1239–1244, 2006.

Wielicki, B. A., Harrison, E. F., Cess, R. D., King, M. D., and Randall, D. A.: Mission to planet Earth: Role of clouds and radiation in climate, Bull. Amer. Meteorol. Soc., 76, 2125–2153, 1995.

Yu, H., Kaufman, Y. J., Chin, M., Feingold, G., Remer, L. A., Anderson, T. L., Balkanski, Y., Bellouin, N., Boucher, O., Christopher, S., DeCola, P., Kahn, R., Koch, D., Loeb, N., Reddy, M. S., Schulz, M., Takemura, T., and Zhou, M.: A review of measurement-based

1   assessments of the aerosol direct radiative effect and forcing, Atmos. Chem. Phys., 6, 613-

2   666, doi:10.5194/acp-6-613-2006, 2006.

3   Zhang, J., Christopher, S. A., Remer, L. A., and Kaufman, Y. J.: Shortwave aerosol radiative

4   forcing over cloud-free oceans from Terra. I: Angular models for aerosols, J. Geophys. Res.,

5   110, D10S23, doi:10.1029/2004JD005008, 2005a.

6   Zhang, J., Christopher, S. A., Remer, L. A., and Kaufman, Y. J.: Shortwave aerosol radiative

7   forcing over cloud-free oceans from Terra. II: Seasonal and global distributions, J. Geophys.

8   Res., 110, D10S24, doi:10.1029/2004JD005009, 2005b.

Table 1. Statistical analysis of the input parameter selection exercise. The correlation coefficient (R), Slope, Bias, and standard deviation (STD) of OMI-CERES TOA SW flux for eight different NN models are presented. These numbers correspond to daily inter-comparison between OMI and CERES TOA SW flux. Data from January 2007 are used for this exercise.

Model	Parameters	R	Slope	Bias	STD (W m^{-2})
a	f_{c_mod}	0.971	0.941	0.051	37.1
b	f_{c_mod}, VZA, RAA	0.979	0.959	0.000	31.4
c	LER, SZA, VZA, RAA	0.979	0.959	-0.030	31.1
d	f_{c_mod}, VZA, RAA, O3	0.980	0.960	-0.009	30.9
e	f_{c_mod}, VZA, RAA, OCP	0.981	0.962	-0.004	30.0
f	f_{c_mod}, VZA, RAA, O3, OCP	0.981	0.963	0.002	29.9
g	f_{c_mod}, VZA, RAA, O3, OCP, PW, Wind	0.982	0.964	0.002	29.2
h	f_{c_mod}, VZA, RAA, O3, OCP, PW, Wind, Chl, LER	0.983	0.967	-0.010	28.3

1   Table 2. Statistical parameters corresponding daily and monthly inter-comparisons of pixel

2   and gridded TOA SW flux data from CERES and OMI.

	N	R	M	I	Bias	STD	EE5%	EE10%	EE15%
Pixel	8109323	0.96	0.96	10.5	-1.4	47.7	30	53	69
Daily									
0.5°	1512726	0.97	0.96	11.2	0.94	34.4	37	62	77
1°	529679	0.98	0.96	11.2	1.0	27.9	43	69	83
2°	168181	0.98	0.96	11.0	0.33	23.7	50	76	87
5°	35454	0.99	0.96	9.2	-1.8	20.3	60	84	92
10°	10834	0.99	0.97	7.0	-0.0	14.6	69	90	97
Monthly									
0.5°	108620	0.99	0.98	6.1	1.5	12.9	74	93	97
1°	28849	0.99	0.98	6.9	1.2	11.4	79	94	98
2°	7642	0.99	0.96	9.8	0.25	6.6	94	99	100
5°	1325	0.99	0.96	9.9	-1.8	7.0	95	99	100

4   *Note: N – Number of pairs, R- correlation coefficient, M- Slope, I- Intercept, Bias – mean of (OMI-CERES in*

5   *Wm^{-2}), STD- standard deviation of (OMI-CERES) in Wm^{-2}, EE –Error Envelope for 5%,10%,15% errors. All*

6   *flux values have units of Wm^{-2}*
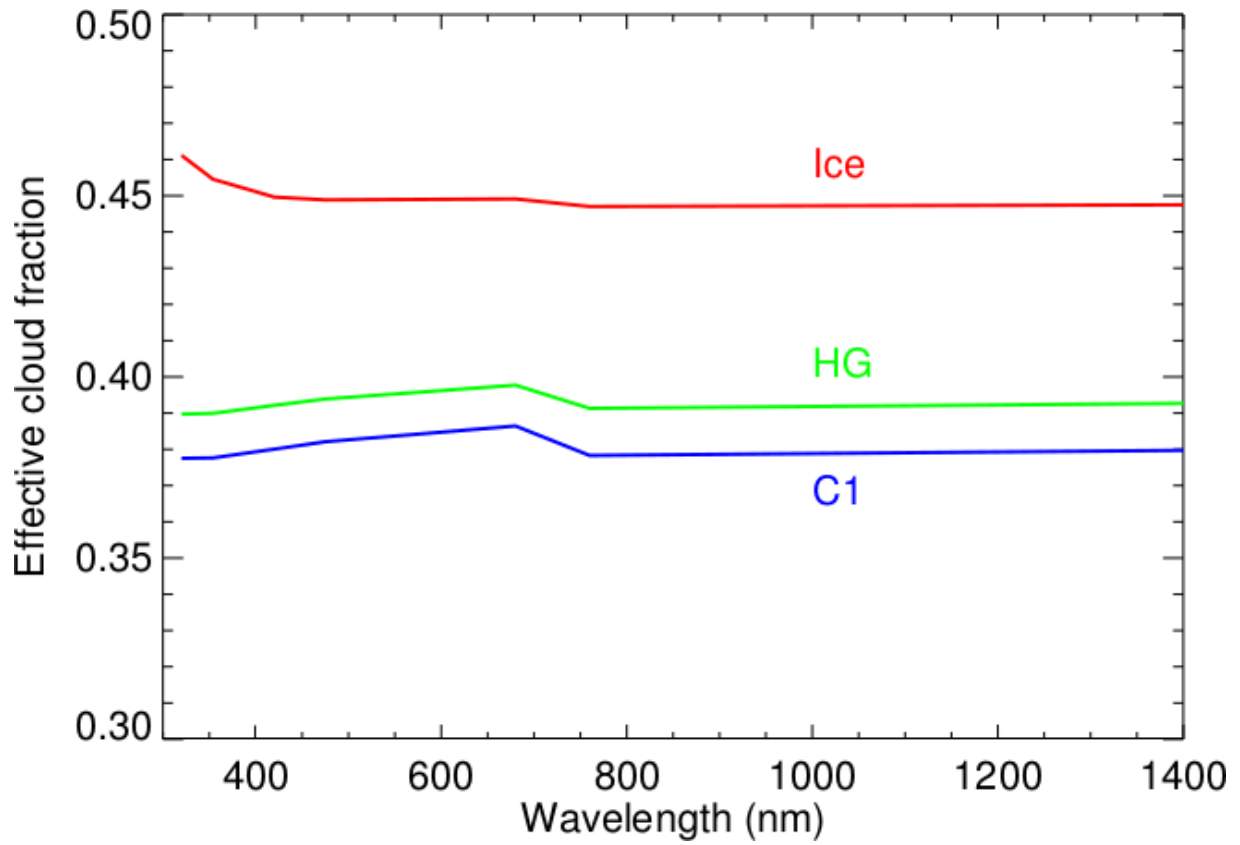
4   Figure 1. The spectral dependence of the effective cloud fraction (f_c) for land, f_g =0.5, SZA =

5   45^0, observation at nadir. Red: ice cloud phase function; green: the Henyey-Greenstein (HG)

6   function; blue: C1 cloud model.
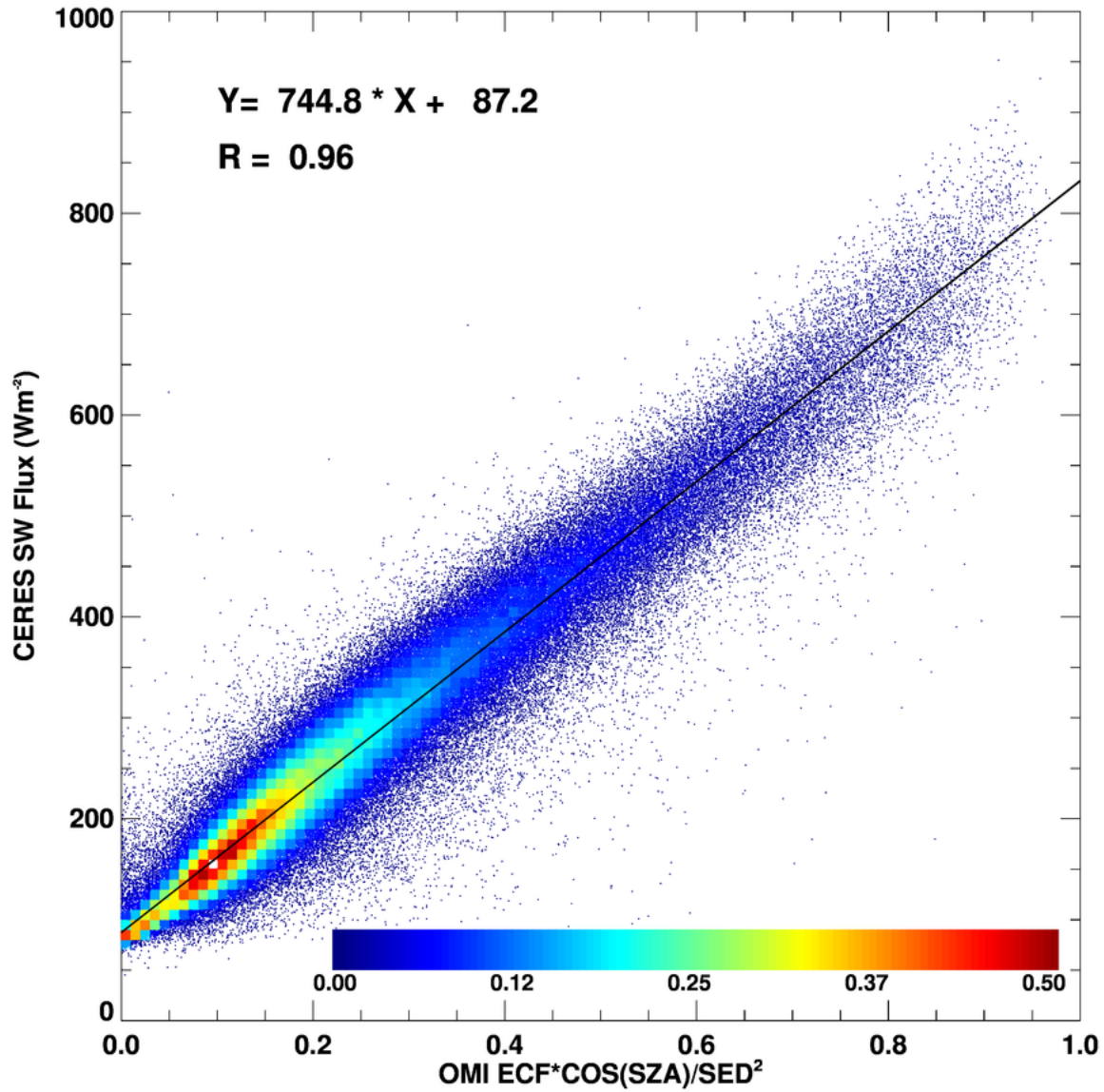
Figure 2. 2D histogram of effective cloud fraction (ECF or f_c) normalized with respect to incoming solar irradiance (i.e., $f_{c\_mod} = ECF * \cos(SZA)/SED^2$) versus CERES TOA shortwave (SW) flux over ocean for January 2007 showing a highly linear relationship. The color bar shows the sample density (normalized, in terms of fractional amount (in %)) for each bin in the collocated data set; when only a single point is in a bin, it is shown as a dark blue dot. R is the linear correlation coefficient. The solid black line is a linear fit to the data.

Neural Network Model	Input Parameters
NNM − 1 [f_c<1.0]	f_{c_mod}, VZA, RAA, OCP, O3, WINDS, PW, CHL, LER
NNM − 2 [f_c≥1.0]	SZA, VZA, RAA, OCP, LER, O3, PW
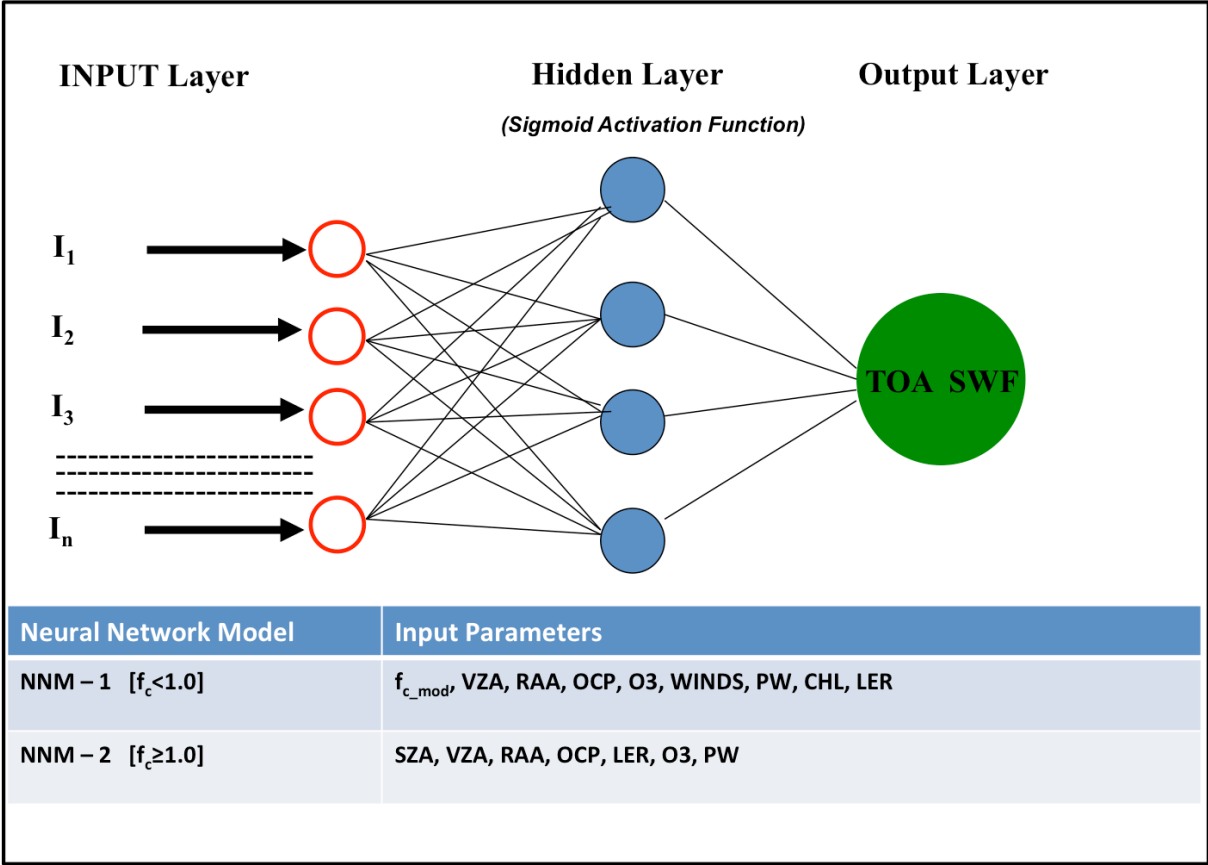
4 Figure 3. A schematic of the neural network model used for estimation of TOA SW flux with

5 OMI UV retrieved parameters. The table in the bottom lists all the input parameters

6 corresponding to two NN models used.
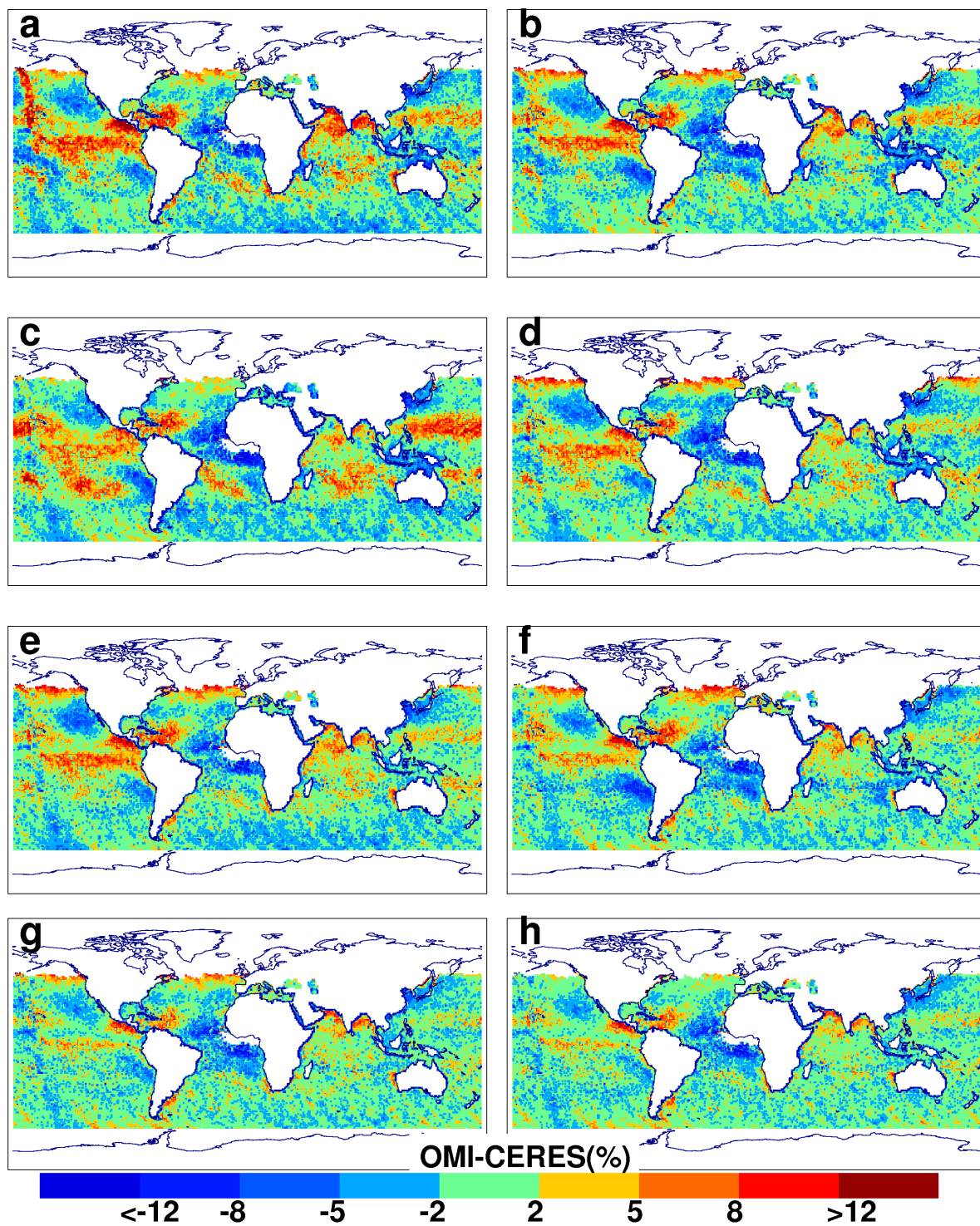
4 Figure 4. Monthly mean (January 2007) maps of OMI minus CERES TOA SW flux (%) for

5 eight different NN models. The letters on the map corresponds to model number in Table 1.
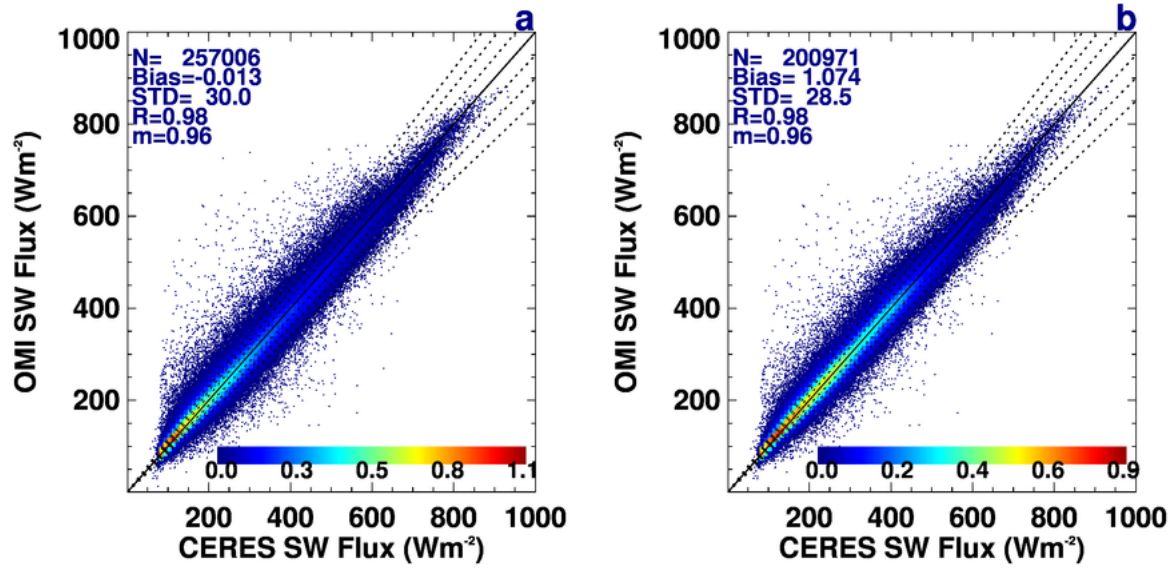
Figure 5. 2D histograms (similar to Figure 2) of daily-mean CERES- and OMI-derived (NN) TOA SW flux for January 2007. a) the NN is trained on and applied to data from January 2007 and compared with CERES data from that month b) the NN is trained using data from January 2007 and applied with input data from January 2006 and compared with CERES data from January 2006. The color bar shows sample density (in fractional (%) amount) of collocated data set (see text for more details). The three dotted lines are 5%, 10% and 15% error envelope lines.
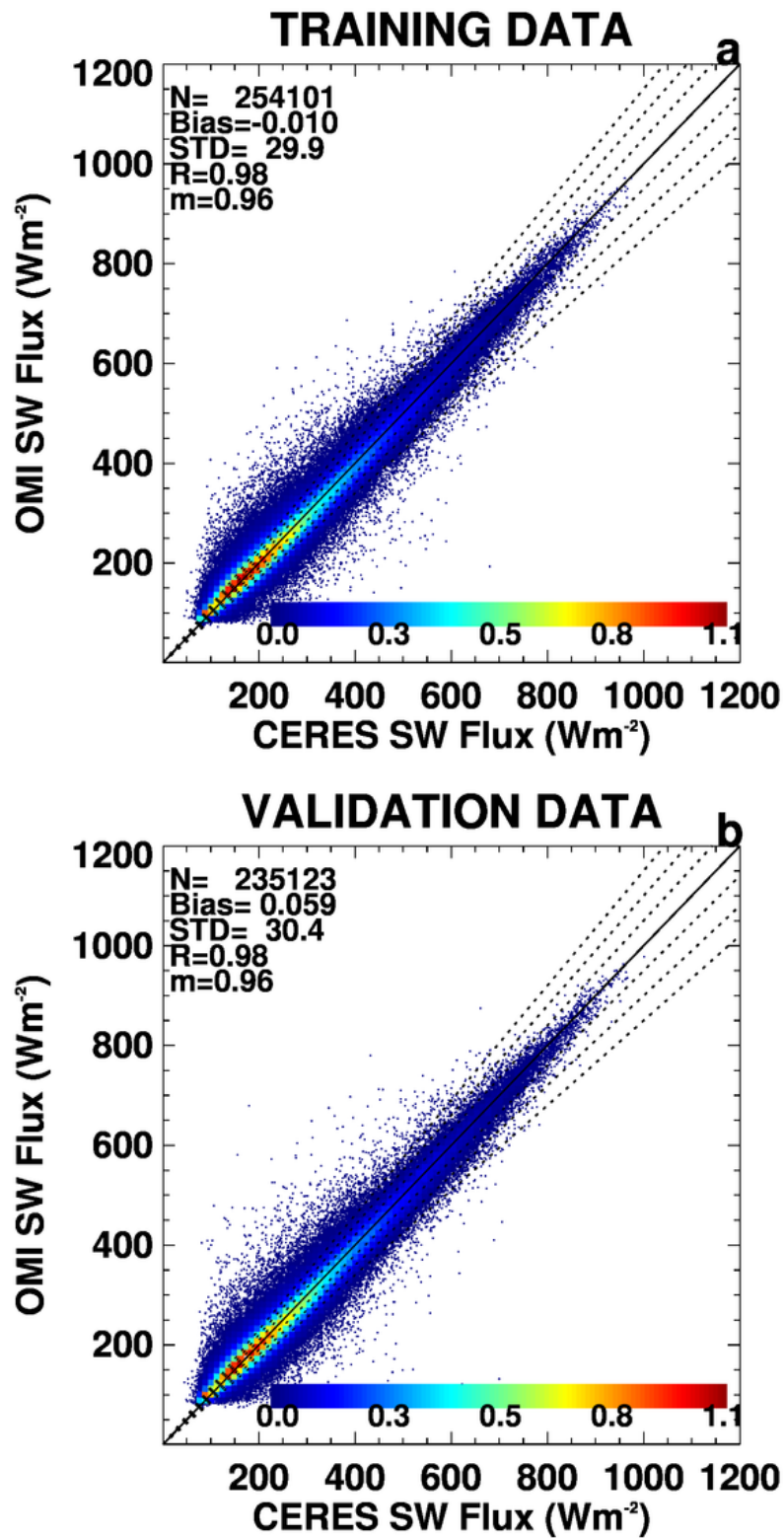
3   Figure 6. 2D histogram similar to Fig. 5 but showing training (top) and validation (bottom)

4   results from the combined all-sky NN models (input parameters listed in Figure 3, model "h"

5   for $f_c<1$ and as in Figure 3 for $f_c>1$) as final selected models for estimation of TOA SW Flux.

1 The data from two NN models have been combined in these plots. These are instantaneous
2 flux values averaged over 1°x1° grid boxes. Data from the 1st day of each month of 2007 are
3 used for training and data from the 16th day of each month of 2007 are used for validation.
4 The three dotted lines are 5%, 10% and 15% error envelope lines.
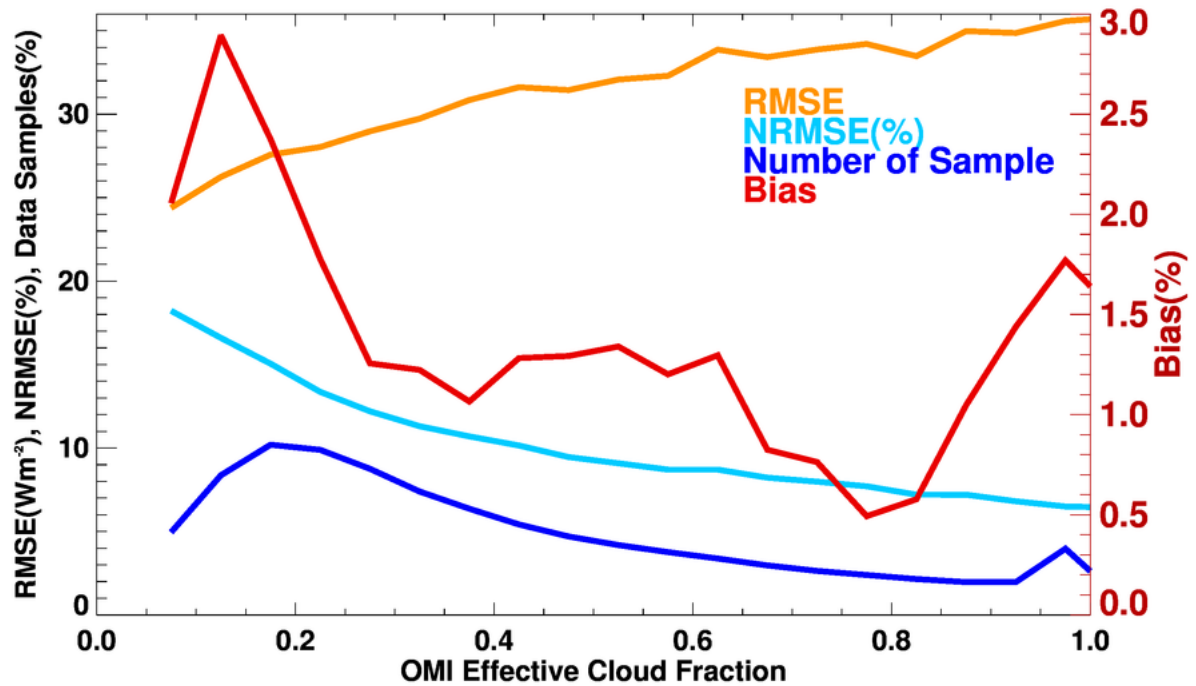
8 Figure 7. Root mean squared errors (RMSE), normalized RMSE (NRMSE in %), data
9 samples (%), and bias (%) in training and validation data sets (same model and data as used in
10 Fig. 6) as a function of effective cloud fraction for the data presented in Figure 4. Model "h"
11 is used to produce these results.

Figure 8. 2D histograms (similar to Fig. 5) of the daily OMI and CERES TOA SW Flux averaged over different spatial grid sizes for July 2007: a) at OMI's native pixel resolution; b) 0.5°x0.5°; c) 1°x1°; d) 2°x2°; e) 5°x5°; and f) 10°x10°. The corresponding statistical parameters are listed in Table 2. Model "h" is used to produce these results. The three dotted lines are 5%, 10% and 15% error envelope lines.
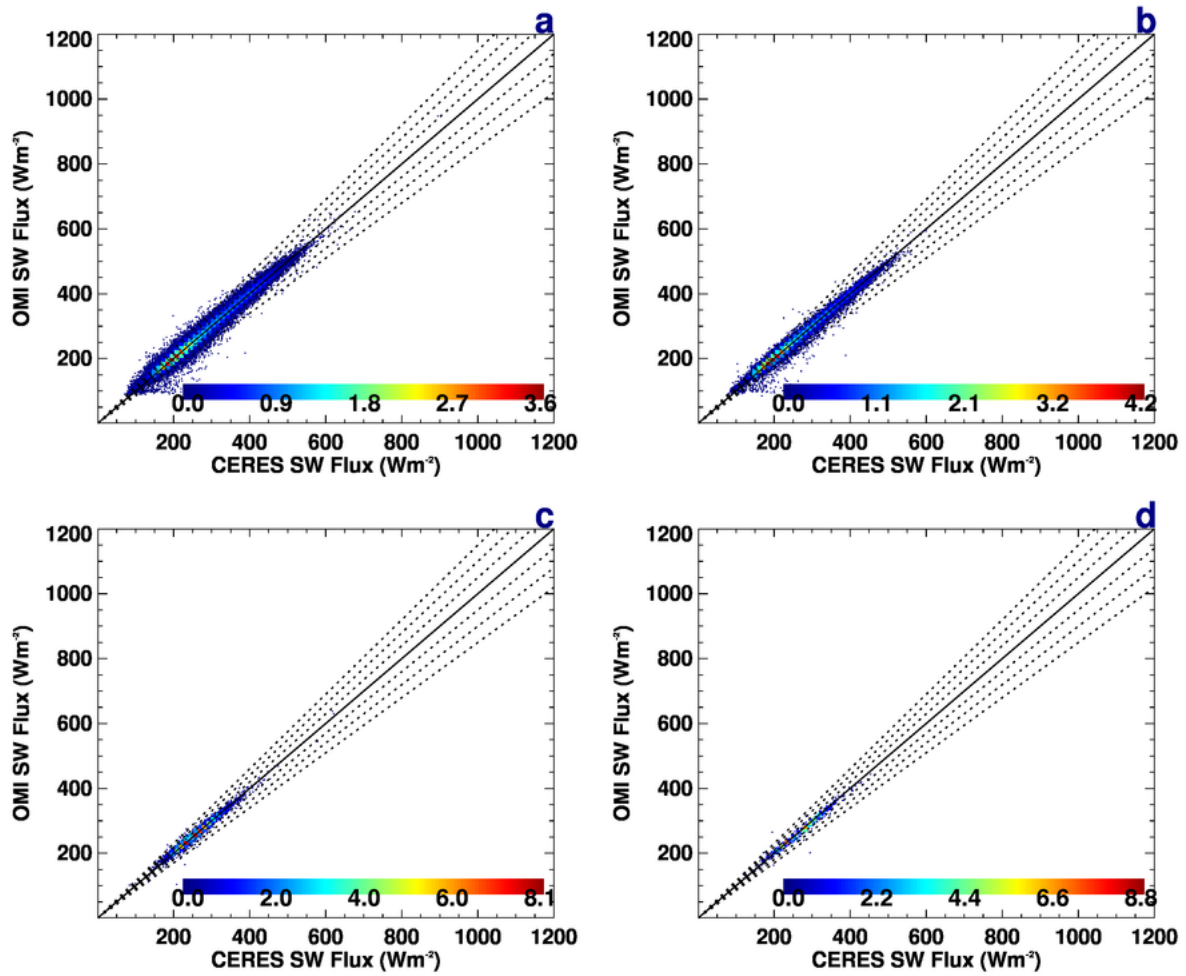
3 Figure 9. Similar to Fig. 8 but for monthly mean data (July 2007) OMI and CERES TOA SW

4 flux averaged over different spatial grid sizes: a) 0.5°x0.5°; b) 1°x1°; c) 2°x2°; d) 5°x5°. The

5 corresponding statistical parameters are listed in Table 2. The three dotted lines are 5%, 10%

6 and 15% error envelope lines.
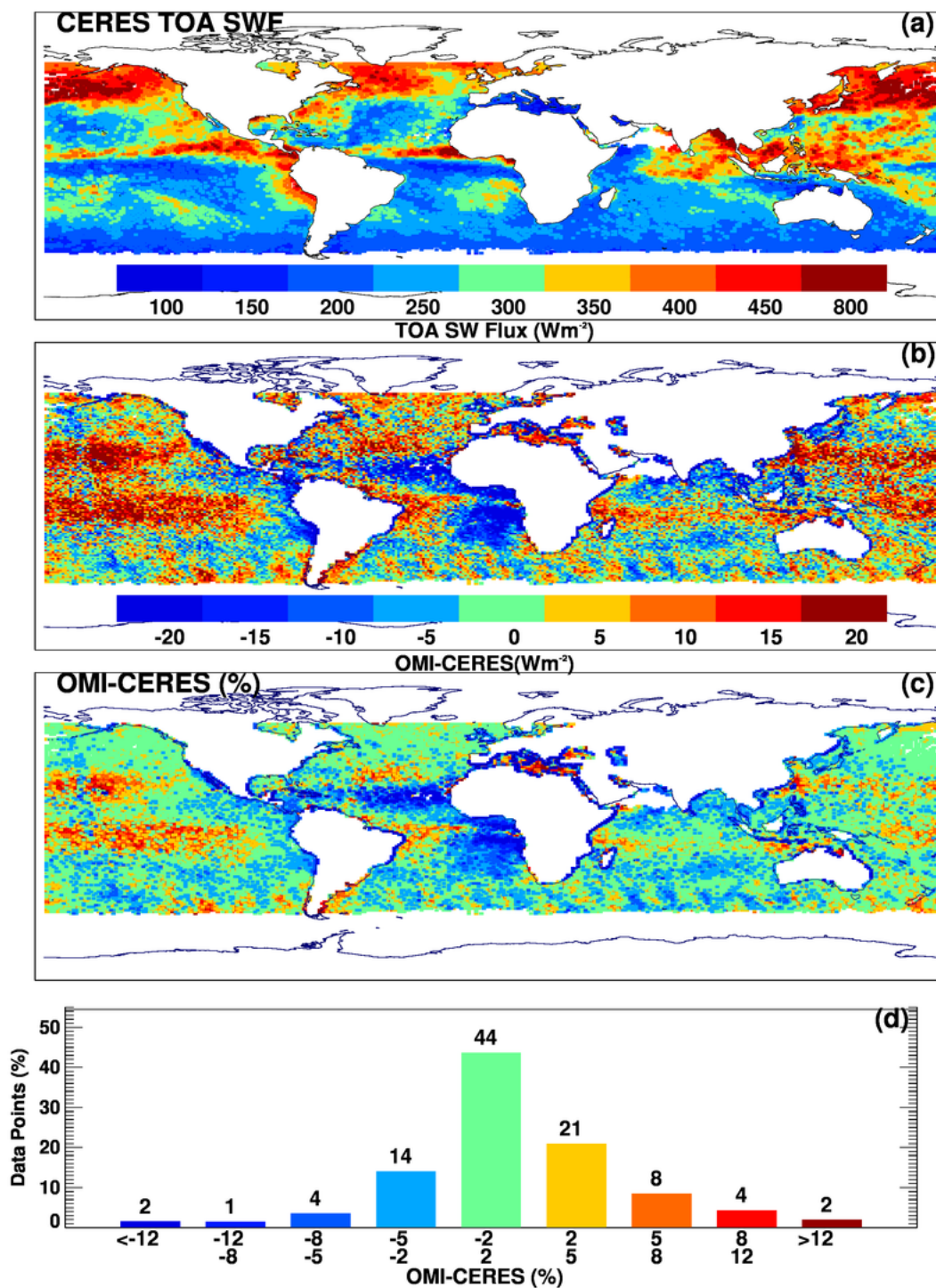
Figure 10. a) Monthly mean (July 2007) spatial distribution of TOA SW flux from CERES; b) OMI-CERES (in Wm⁻²); c) OMI-CERES (%); d) histogram of OMI-CERES (%). The colors in (c) correspond to histogram colors in (d).
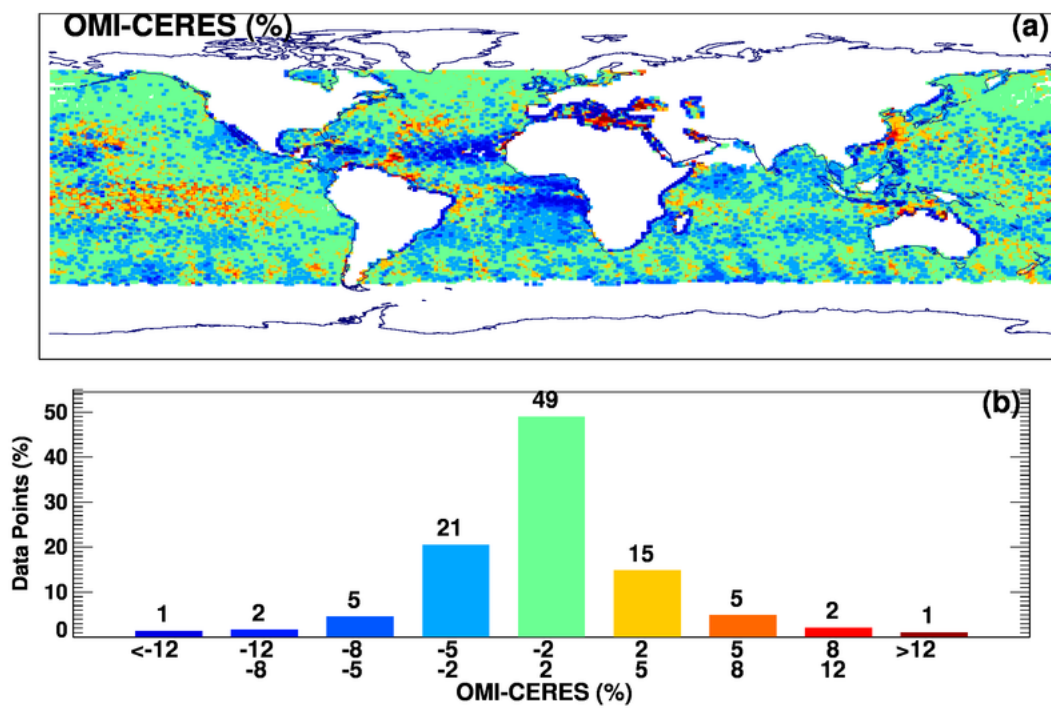
Figure 11. Similar to Fig. 10c and d, but with a NN trained using data from the OMI cloud
O$_2$-O$_2$ product for July 2007.
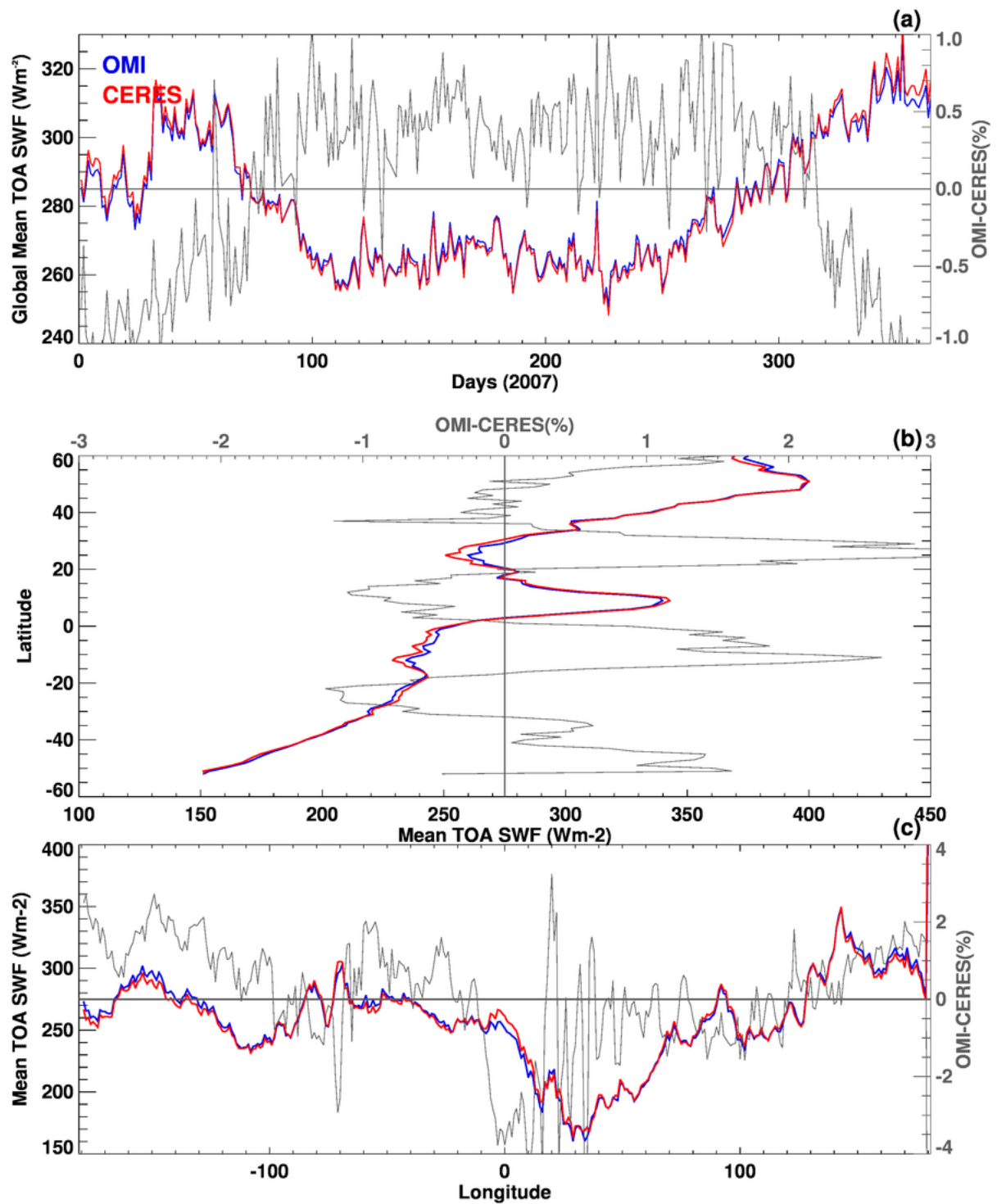
3   Figure 12. a) The daily global mean time series of TOA SW fluxes from the OMI NN and

4   CERES and OMI-CERES (%) on the secondary y-axis; b) Mean TOA SWF from CERES and

5   OMI averaged along each latitude belt, and OMI-CERES (%) on the secondary x-axis; c)

6   same as b, but along longitude belts. The data used in b and c are from July 2007.
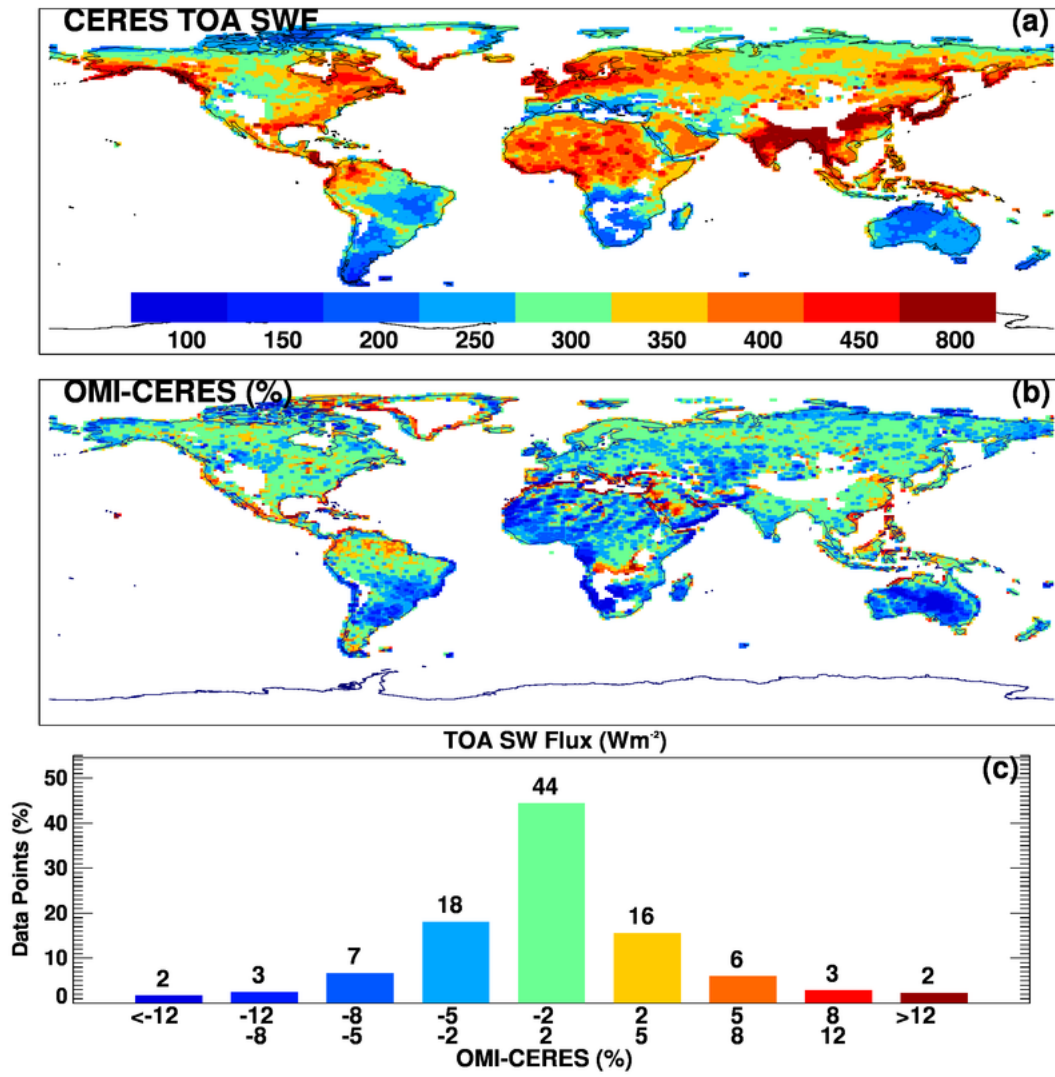
4   Figure 13. Similar to Fig. 10 (a, c, d) except over land for July 2007.